CORA Cork Open Research Archive
Cartlann Taighde Oscailte Chorcaí

Title	Wave power extraction from a hybrid oscillating water column-oscillating buoy wave energy converter
Authors	Cui, Lin;Zheng, Siming;Zhang, Yongliang;Miles, Jon;Iglesias, Gregorio
Publication date	2020-08-23
Original Citation	Cui, L., Zheng, S., Zhang, Y., Miles, J. and Iglesias, G. (2020) 'Wave power extraction from a hybrid oscillating water column-oscillating buoy wave energy converter', Renewable and Sustainable Energy Reviews, 135, 110234 (19pp). doi: 10.1016/j.rser.2020.110234
Type of publication	Article (peer-reviewed)
Link to publisher's version	10.1016/j.rser.2020.110234
Rights	© 2020, Elsevier B.V. All rights reserved. This manuscript version is made available under the CC BY-NC-ND 4.0 license. - https://creativecommons.org/licenses/by-nc-nd/4.0/
Download date	2026-11-02 00:52:24
Item downloaded from	https://hdl.handle.net/10468/10414

UCC
University College Cork, Ireland
Coláiste na hOllscoile Corcaigh

Title:

Wave power extraction from a hybrid oscillating water column-oscillating buoy wave energy converter

Journal:

Renewable and Sustainable Energy Reviews

Author names and affiliations:

Lin Cui[a,e], Siming Zheng[b,*], Yongliang Zhang[c], Jon Miles[b], Gregorio Iglesias[b,d]

a College of Shipbuilding Engineering, Harbin Engineering University, Harbin, 150001, China
b School of Engineering, Computing and Mathematics, University of Plymouth, Drake Circus, Plymouth PL4 8AA, United Kingdom
c State Key Laboratory of Hydroscience and Engineering, Tsinghua University, Beijing, 100084, China
d Centre for Marine Renewable Energy Ireland (MaREI), Environmental Research Institute & School of Engineering, University College Cork, Ireland
e National Ocean Technology Center, Tianjin, 300112, China

* Corresponding author:

Siming Zheng (siming.zheng@plymouth.ac.uk)

https://doi.org/10.1016/j.rser.2020.110234

Received 28 July2019;
Received in revised form 3 August2020;
Accepted 8 August2020

Wave power extraction from a hybrid oscillating water column-oscillating buoy wave energy converter

Abstract

Oscillating water column (OWC) devices and oscillating buoys (OBs) are two of the main types of wave energy converters (WECs). In this paper a hybrid oscillating water column-oscillating buoy wave energy converter is proposed, which we have named OWCOB. The oscillating buoy is hinged at the outer wall of the oscillating water column. As waves propagate through the OWCOB, the water column within the OWC chamber moves up and down, producing air flow to propel a turbine. Meanwhile, the oscillation of the OB drives a separate hydraulic system. To solve the wave diffraction and radiation problems of the OWCOB and investigate its energy capture performance, an analytical model is developed based on linear potential flow theory and the eigenfunction matching method. Assuming that the PTOs of the OWC and OB are both linear, the wave power extraction of the OWCOB is evaluated in the frequency domain. Of the two configurations considered, the OWCOB with the OWC opening waveward and the OB hinged leeward is found to have a broader primary frequency band of wave power capture compared to the OWCOB with the OWC opening and the OB on the same side. Further, a thorough sensitivity analysis of power capture is carried out considering the main design parameters (size and submergence of the OWC opening, distance between the OWC and the OB, OB hinge elevation, OB radius), which can form the basis of an optimisation study for a particular wave climate. Importantly, we find that the OWCOB performs generally better than stand-alone OWCs and OBs, not least in terms of frequency bandwidth.

Keywords

Wave power; Wave energy; Wave radiation; Potential flow theory; Oscillating water column; Oscillating buoy

1 Introduction

To meet the rising demand for energy in coastal and offshore regions, and also converge towards a net zero-carbon economy, more and more attention is being paid to seeking renewable energy from the ocean. Ocean energy includes wave power, tidal power, and ocean thermal energy, of which wave power offers the highest energy density [1].

The global wave energy resource is estimated at 17 TW h/year [2], with the largest values of average wave power occurring in the mid-latitudes (between 30° and 60°) [3]. In order to exploit this vast resource, various wave energy conversion technologies have been developed [1, 4-7]. Among these, Oscillating Water Columns (OWC) and nodding devices are two of the main types.

An OWC is composed of a partially submerged rigid chamber with an opening under the water level. As ocean waves propagate, the water column enclosed by the chamber oscillates up and down, driving air through a turbine installed on the chamber and, in the process, generating electricity with a generator [7, 8]. OWCs can be generally classified by location into shore-attached devices and offshore devices.

Evans and Porter [9] proposed a 2D analytical model to solve the hydrodynamics of a

generalized shore-attached OWC, which consists of a thin vertical surface-piercing barrier next to a vertical wall. In order to deal with the singular behavior of the velocity field at the edge of the thin barrier, an integral equation for the horizontal velocity across the opening under the thin barrier was utilized. Rezanejad et al. [10] considered the effect of a stepped bottom topography on the efficiency of a shore-attached OWC. It was found that the existence of an artificial step at the sea bottom with proper tuning could result in a significantly increased capacity of wave power absorption. Ning et al. [11] developed a 2D fully nonlinear numerical wave tank (NWT) based on a time-domain higher-order boundary element method (BEM) and investigated the performance of a shore-attached OWC device. The numerical results indicated that the maximum surface-elevation inside the OWC chamber occurred at a lower frequency compared to the resonant frequency of the chamber. The hydrodynamic efficiency increased with the wave amplitude for weaker wave nonlinearity. Zhang et al. [12] developed an immersed boundary method model based on a two-phase level set with the global mass correction to simulate wave interaction with a shore-attached OWC. The detailed flow field in the air and water, pressure distribution, surface elevation, and vorticity strength demonstrated in their study elucidated the complicated physical process related to OWC performance. Pereiras et al. [13] described a methodology to match a non-linear turbine to the characteristics of an OWC device for an optimal energy transfer. The non-linearity of the turbine was considered, and the performance of the OWC was obtained from experimental tests (or validated numerical model). In order to determine the optimum damping accounting for the wave climate variability, López et al. [14] evaluated the pneumatic power matrices corresponding to different values of turbine-induced damping by using a 2D RANS-VOF NWT model. With this optimization methodology, the annual energy output of the OWC could be improved significantly.

In addition to the analytical and numerical work, experimental tests have also been widely adopted to study the performance of a 2D shore-attached OWC. Morris-Thomas et al. [15] utilized both numerical and experimental tests to examine energy efficiencies for power take-off of a shore-attached OWC. They found the hydrodynamic performance of the OWC was marginally improved with rounded rather than rectangular aperture shape of the submerged front wall. Viviano et al. [16] carried out large scale experiments to study wave reflection and loading on an OWC caisson breakwater under random wave conditions. Recent experimental load tests of three breakwater-based OWC chamber regimes, i.e., closed chamber, fully open condition, and operating condition, in both regular and irregular wave conditions, were reported by Pawitan et al. [17]. In laboratory tests of OWC devices, air compressibility is often neglected – which simplifies the model construction. The effects of this neglect on the performance as measured in laboratory tests were investigated in a recent work by López et al. [18]. The variation of the energy conversion performance of an OWC as a function of the site was also recently investigated [19].

Apart from the traditional single-chamber coast or breakwater based OWC, an OWC with a dual chamber was also proposed to enhance power extraction [20-22]. Other researchers have investigated a U-OWC plant, which includes an additional vertical duct in front of a traditional OWC [23-26]. The resonance conditions of the U-OWC can be reached without phase control devices. Furthermore, the amplitude of the pressure oscillation in the air pocket was increased, which enhanced the performance of the plant.

When the dimension of the OWC along the coast or breakwater is comparable to the wavelength, 3D wave diffraction and radiation problems should be considered. Martins-rivas and Mei [27] evaluated the wave power extraction of an OWC attached to the tip of a breakwater. The

wave power absorption was found to be independent of the incident wave direction. Martins-rivas and Mei [28] considered a coast integrated OWC, whose chamber is a vertical cylindrical shell half embedded in a vertical coast. The analysis showed that the power captured by the OWC was doubled due to the wave reflection at the vertical coast. Subsequently, Lovas et al. [29] generalized the model [28] to an OWC integrated into a coastal corner. More recently, their model was also extended by Zheng et al. [30] and Zheng et al. [31] to a general case without the thin-wall restriction, i.e., considering the thickness of the OWC chamber wall. For a given outer radius of the chamber, the thinner the chamber wall, the higher and broader the main peaks of the wave capture factor frequency response. A finite-element model (FEM)-based numerical simulation and experimental tests were carried out by Howe and Nader [32] to investigate the hydrodynamics of a Bent Duct OWC device implemented in a flat-faced breakwater. OWCs with both rectangular and circular cross sections were examined, and the variation in inlet geometry demonstrated low deviations in the results.

Unlike the shore-attached OWC as reviewed above, the offshore OWC allows water waves to pass around and/or underneath the device walls. There have been extensive analytical studies for a stand-alone offshore OWC. As early as 1978, Evans [33] considered the 2D problem of regular waves incident upon an offshore OWC, which was composed of a pair of thin vertical closely-spaced plates, in the framework of linear potential flow theory. The water column enclosed by the plates was assumed to move like a rigid piston in the problem. It was shown that for the 2D offshore OWC consisting of two plates of equal length, the maximum analytical efficiency was 50%. Later, Evans [34] generalized the previous theory by taking into account the spatial variation of the water column surface. To analyze the performance of a heave-only offshore floating OWC, Luo et al. [35] developed a 2D fully nonlinear NWT with a dynamic mesh based on the commercial software FLUENT. In addition to the natural frequency of the OWC, another resonant frequency, i.e., the natural frequency of the chamber, was observed for the heave-free floating OWC device. Therefore, the frequency bandwidth of high efficiency can be expanded by adjusting the turbine damping coefficient and/or the stiffness of the mooring spring, and more energy could be harnessed from ocean waves with a broader banded spectrum. Elhanafi et al. [36] applied a fully nonlinear CFD model based on the 2D RANS equations with a VOF surface capturing scheme to study the effects of the underwater geometry on the power extraction of a fixed offshore OWC. For a given front lip draught, the overall power extraction efficiency can be significantly improved by increasing the submergence of the rear lip. More recently, He et al. [37] presented a multi-parameter analytical study of the hydrodynamic performance of a pile-supported offshore OWC working as a breakwater. The analytical results revealed that a satisfactory wave transmission can be obtained by an optimization towards maximum power extraction. If an optimization strategy towards minimum wave transmission was employed, a smaller wave transmission coefficient was achieved, but this was at the expense of a significant reduction in wave power absorption. Studies of an offshore 2D OWC with more complicated shapes, e.g., a dual-chamber OWC, can be found in [38-40].

In order to evaluate the power extraction from a 3D offshore OWC consisting of a thin-walled hollow cylinder, Evans and Porter [41] proposed a simple analytical model based on the theory of pressure distributions and the accurate Galerkin method, which had been previously adopted for solving the hydrodynamic problems of the 2D shore-attached OWC [9]. Sheng et al. [42] treated an offshore OWC as a two-body system, with the OWC chamber itself and an imaginary “piston” replacing part of the water at the free surface inside the chamber. A BEM-based numerical model

was applied to solve the hydrodynamics of this two-body system in the frequency domain. After implementing the time-domain analysis based on Cummins-Ogilvie's equation, the effect of a nonlinear PTO system was considered. The numerical results for a bottom-fixed OWC were in excellent agreement with physical tests [43]. Nader [44] developed a fully numerical 3D FEM model based on the inviscid potential flow theory. Hydrodynamic and energetic properties were investigated for an offshore fixed/floating OWC, and an array of such offshore fixed OWCs. Analytical study of wave power extraction of free-floating OWCs was carried out by Konispoliatis and Mavrakos [45]. For an offshore OWC, especially a fixed one, a certain supporting structure where the OWC is installed is generally required. Deng et al. [46] considered an OWC supported by a coaxial tubular structure. In their model, there was an opening at the side wall below the (still) water level, extending from a given depth to the sea bed. The analytical investigation indicated that the optimal performance in terms of power absorption was achieved when incident waves propagated perpendicularly to the opening. The hydrodynamic performance of other types of offshore OWCs, e.g., backward-bent duct buoy (BBDB) and Spar-buoy, was reported in [47-51].

The nodding device is a WEC that consists of one or more floats hinged on either an offshore structure or coastline and utilizes the rotation of these floats to drive the hydraulic PTO system at the hinges to generate electricity. Compared to the extensive studies on the OWCs, there are relatively few studies dealing with nodding devices. The Salter's Duck [52], which was proposed by Stephen Salter, may well be one of the most famous nodding WECs. An experimental study in a narrow wave tank demonstrated that the power absorption efficiency of Salter's Duck could be more than 90% [53]. Cruz and Salter [54] utilized a commercial BEM package to examine the impact of the rotational axis position and the submergence ratio on the power extraction of a modified Salter Duck device. The axis position was found to significantly affect the performance of the device. The SDE device and the Wavestar are another two examples of nodding WECs [4, 55]. The SDE WEC is composed of a flat float articulated on the coast and a hydraulic system installed at the hinge to change the float mechanical motion into electricity. Haren [56] presented a numerical model of 2D potential flow theory of the hydrodynamics of a floating plate articulated on a vertical wall, which was similar to the concept of SDE. It was shown that all the incident wave power could be captured for some specified wave conditions if the plate and PTO system were well designed. In order to overcome the problem of an efficiency decline induced by the tidal range, a unique rotating device between the coast and the float was introduced by Yang et al. [57]. Wavestar [55] is mainly composed of a platform and multiple nodding cylindrical floats hinged around it. Jakobsen et al. [58] applied both experiments and inviscid BEM based numerical simulations to determine the hydrodynamic and dynamic loads on the Wavestar WEC. The results of the slamming pressures on the shell indicated that the asymptotic theory for cylinders may also be applicable to hemispheres. Ransley et al. [59] reproduced the pressure distribution and loading on the Wavestar device by running a fully nonlinear, coupled model developed with open-source CFD software, OpenFOAM. The comparison between the physical and numerical results for the freely pitching cases showed close agreement. The construction cost and system complexity of the Wavestar may be high due to the requirement of a large supporting platform. This problem may be overcome by integrating the nodding device with an offshore OWC.

Zheng and Zhang [60] proposed a hybrid WEC, which is composed of a long fixed, inverted flume with a bottom hole acting as an OWC and a long floating cube hinged on the OWC working as an oscillating float. Both the OWC and the rotational motion of the float are utilized to capture

wave power. Analytical studies in the 2D Cartesian coordinate system demonstrated that a positive influence of the hydrodynamic interaction between the float and the OWC on wave power extraction of the hybrid WEC can be achieved for certain wave conditions. Meanwhile, another hybrid WEC that consists of a hollow cylinder working as an OWC and several oscillating floats hinged around it was proposed and studied by a 3D semi-analytical model [61]. The results indicated that the hybrid WEC could lead to a wider bandwidth of frequency response with a higher maximum power capture factor compared with the isolated OWC and hinged floats.

In this paper, a hybrid WEC consisting of an OWC with an OB hinged at the outer wall of the OWC is considered, which is referred to as an OWCOB hereafter. The hinged OB may be considered as a nodding device. Unlike previously proposed hybrid WECs, the OWC in the present OWCOB is encased in a tubular structure, hence the device can be easily integrated into marine structures such as piles and offshore wind turbines. When water waves propagate through the OWCOB, the water column enclosed by the OWC chamber moves up and down, and a PTO device such as an air turbine installed at the top of the OWC is driven to extract wave power. Meanwhile, a second PTO such as a hydraulic system installed at the hinge can be driven by the rotation of the OB to capture power as well. In order to investigate the power extraction of such a device, a 3D analytical model is developed here based on linear potential flow theory and eigenfunction matching method.

In previous work it was shown that a tubular structure supported OWC with its opening deployed on the waveward side had optimal performance in wave power extraction [46]. For this reason, the investigation in this paper is concerned with an OWCOB with the OWC opening to waveward, unless otherwise stated.

The rest of this paper is organized as follows. Section 2 describes the analytical model, including the solutions of wave diffraction and radiation problems, the expressions of wave excitation volume, forces and hydrodynamic coefficients, and the method to evaluate the wave power absorption. The model validation is presented in Section 3. In Section 4 the model is applied to examine the effect of the configuration of the OWCOB and the main design parameters (e.g., the opening size and position) on wave power absorption. Conclusions are drawn in Section 5.

2 Mathematical model

Figure 1 shows a sketch of an OWCOB in water of constant depth h. The OWCOB is composed of an OWC encased in a tubular structure and an OB hinged at the side of the OWC. The elevation of the hinge above the water level is denoted as d. The side wall of the tubular structure is partially open at depth d_1 with an opening height of d_0 and an opening angle $\alpha=\upsilon\pi$ in the horizontal plane. If the starting side of the opening in the horizontal plane is denoted by $\theta_1=\gamma$, then the horizontal axis of symmetry of the opening (the dash-dot line in blue, Fig. 1b) is the polar line $\theta_1=\gamma+\alpha/2$. R_1 and R_i denote the outer and inner radii of the tubular cross-section, respectively. The radius and draught of the OB are denoted by R_2 and d_2, respectively. The horizontal distance between the centres of the OWC and the OB is represented by D. There are two PTO systems: a pneumatic PTO system consisting of an air turbine located at the top of the OWC, and a hydraulic PTO system consisting of a cylinder and a closed oil circuit at the hinge. As waves propagate through the OWCOB, the two PTO systems are driven by the motion of the water column enclosed by the OWC chamber and the rotation of the OB relative to the hinge, respectively, to capture power from the waves.

In order to describe the problem mathematically, a Cartesian coordinate system $Oxyz$ is defined with the mean water level being the z=0 plane, the Oz-axis pointing vertically upward along the

vertical axis of the tubular structure, and the *Ox*-axis pointing from the OWC towards the OB horizontally (see Fig.1b). Additionally, two local cylindrical coordinate systems $O_1r_1\theta_1z$ and $O_2r_2\theta_2z$ are introduced with the origins at the intersections between the vertical axes of the OWC and OB and the mean water level.

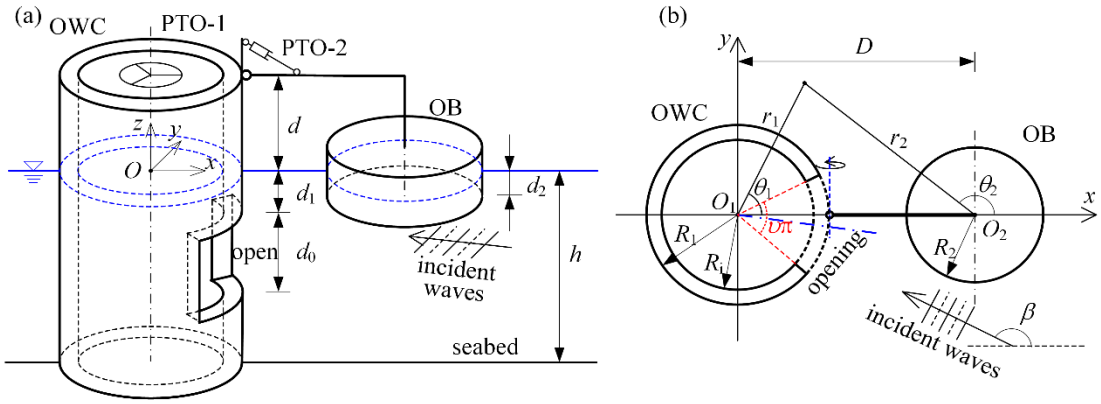


Fig. 1. Sketch of an OWCOB: (a) bird view; (b) top view.

When the OWCOB is subjected to monochromatic waves of small amplitude A, angular wave frequency ω and direction β (Fig. 1b), a velocity potential $\mathrm{Re}[\Phi(x,y,z)e^{-i\omega t}]$ may be used to describe the flow field assuming that water is inviscid and incompressible. Here, Φ is the complex spatial velocity potential, i denotes the imaginary unit, and t represents time. Φ may be decomposed into an incident wave spatial potential, Φ_I, a diffracted wave spatial potential, Φ_D, and a radiated wave spatial potential:

$$\Phi = \Phi_\mathrm{I} + \Phi_\mathrm{D} + \sum_{n=1}^{4} \dot{X}_n \Phi_n \,, \tag{1}$$

where $\dot{X}_n$ denotes the complex amplitude of the air pressure inside the OWC chamber for n=1 ($\dot{X}_1$=p) and the OB velocity oscillation in mode n for n = 2, 3, 4, which represent surge, heave and pitch relative to the mass centre of the OB, respectively. Here the mass centre of the OB is assumed to coincide with the centroid and its position in the local cylindrical coordinate system $O_2r_2\theta_2z$ can be expressed as (r_2=0, z =z_0). Φ_n represents the radiated spatial potentials induced by unit air pressure oscillation inside the OWC chamber (n=1) and that due to unit amplitude velocity oscillation of the OB in mode n (n = 2, 3, 4). The Laplace equation in the water domain and a radiation condition at infinity are satisfied by both Φ_D and Φ_n.

For the sake of simplicity, the scattering velocity potential Φ_0 is adopted to represent the sum of the incident and diffracted velocity potentials, i.e., Φ_0=Φ_I +Φ_D.

2.1 Boundary conditions

The boundary conditions that Φ_χ (χ=0, 1, …, 4) should satisfy are as follows:

$$\frac{\partial \Phi_\chi}{\partial z} = 0 \,, \quad z\text{=-}h, \tag{2}$$

$$\frac{\partial \Phi_\chi}{\partial z} = 0, \quad r_1 \in [R_i, R_1],\ \theta_1 \in [\gamma, \gamma+\upsilon\pi],\ z=-h_1 \text{ and } -d_1, \tag{3}$$

$$\frac{\partial \Phi_\chi}{\partial z} = \delta_{\chi,3} - \delta_{\chi,4} r_2 \cos\theta_2, \quad r_2 \in [0, R_2],\ \theta_2 \in [0, 2\pi],\ z= -d_2, \tag{4}$$

$$\frac{\partial \Phi_\chi}{\partial z} - \frac{\omega^2}{g}\Phi_\chi = 0, \quad r_n \in [R_n, \ \infty),\ \theta_n \in [0, 2\pi],\ z=0, \tag{5}$$

$$\frac{\partial \Phi_\chi}{\partial z} - \frac{\omega^2}{g}\Phi_\chi = \delta_{\chi,1}\frac{\mathrm{i}\omega}{\rho g}, \quad r_1 \in [0, R_i],\ \theta_1 \in [0, 2\pi],\ z=0, \tag{6}$$

$$\frac{\partial \Phi_\chi}{\partial \theta_1} = 0, \quad r_1 \in [R_i, R_1],\ \theta_1=\gamma \text{ and } \gamma+\upsilon\pi,\ z \in [-h_1, -d_1], \tag{7}$$

$$\frac{\partial \Phi_\chi}{\partial r_1} = 0, \quad r_1=R_i \text{ and } R_1,\ \theta_1 \notin [\gamma, \gamma+\upsilon\pi],\ z \in [-h_1, -d_1], \tag{8}$$

$$\frac{\partial \Phi_\chi}{\partial r_1} = 0, \quad r_1=R_i \text{ and } R_1,\ \theta_1 \in [0, 2\pi],\ z \in [-h, -h_1], \tag{9}$$

$$\frac{\partial \Phi_\chi}{\partial r_1} = 0, \quad r_1=R_i \text{ and } R_1,\ \theta_1 \in [0, 2\pi],\ z \in [-d_1, 0], \tag{10}$$

$$\frac{\partial \Phi_\chi}{\partial r_2} = \delta_{\chi,2}\cos\theta_2 + \delta_{\chi,4}\left(z - z_0\right)\cos\theta_2, \quad r_2= R_2,\ \theta_2 \in [0, 2\pi],\ z \in [-d_2, 0], \tag{11}$$

where $h_1=d_1+d_0$, ρ is the water density, g is the gravity acceleration, and $\delta_{\chi,n}$ is the Kronecker delta.

2.2 Expressions of wave scattering/radiated potentials

The water domain can be divided into four regions: I, inner region enclosed by the tubular structure, i.e., $r_1 \in [0, R_i]$, $\theta_1 \in [0, 2\pi]$, $z \in [-h, 0]$; II, opening region with a fan-shaped cross-section, i.e., $r_1 \in [R_i, R_1]$, $\theta_1 \in [\gamma, \gamma+\upsilon\pi]$, $z \in [-h_1, -d_1]$; III, region under the OB, i.e., $r_2 \in [0, R_2]$, $\theta_2 \in [0, 2\pi]$, $z \in [-h, -d_2]$; and IV, outer region, i.e., the rest of the water domain. Φ_χ (χ=0, 1, …, 4) in these four regions are denoted as Φ_χ^{in}, Φ_χ^{open}, Φ_χ^{OB} and Φ_χ^{out}, respectively, and their expressions can be written as follows.

I, inner region:

$$\Phi_\chi^{\text{in}}\left(r_1, \theta_1, z\right) = \sum_{m=-\infty}^{\infty}\sum_{l=0}^{\infty}\frac{\tilde{I}_m\left(k_l r_1\right)}{k_l \tilde{I}'_m\left(k_l R_i\right)} A_{m,l}^{(\chi)} Z_l\left(z\right)\mathrm{e}^{\mathrm{i}m\theta_1} - \frac{\mathrm{i}\delta_{\chi,1}}{\rho\omega}, \tag{12}$$

where $A_{m,l}^{(\chi)}$ are the unknown coefficients to be determined,

$$\tilde{I}_m\left(k_l r_1\right)=\begin{cases} J_m\left(k_l r_1\right), & l=0 \\ I_m\left(k_l r_1\right), & l\neq 0 \end{cases}, \tag{13}$$

in which J_m and I_{m} denote the Bessel function and the modified Bessel function of the first kind and order m, respectively. k_0 is the wave number and k_l (l>0) is the eigenvalue given by,

$$\omega^2=-gk_l\tan\left(k_l h\right), \qquad l=1, 2, 3\ \ldots \tag{14}$$

$$Z_0\left(z\right)=N_0^{-0.5}\cosh\left[k_0\left(z+h\right)\right];\ \ Z_l\left(z\right)=N_l^{-0.5}\cos\left[k_l\left(z+h\right)\right]; \tag{15}$$

where

$$N_0=\frac{1}{2}\left[1+\frac{\sinh\left(2k_0 h\right)}{2k_0 h}\right],\ \ N_l=\frac{1}{2}\left[1+\frac{\sin\left(2k_l h\right)}{2k_l h}\right]. \tag{16}$$

II, opening region with a fan-shaped cross section:

$$\Phi_\chi^{\mathrm{open}}\left(r_1,\theta_1,z\right)=\sum_{m=0}^{\infty}\left[F_{m,0}^{\chi}\left(r_1\right)+\sum_{l=1}^{\infty}\left(C_{m,l}^{(\chi)}\frac{I_{\frac{m}{\upsilon}}\left(\beta_{1,l}r_1\right)}{I_{\frac{m}{\upsilon}}\left(\beta_{1,l}R_1\right)}+D_{m,l}^{(\chi)}\frac{K_{\frac{m}{\upsilon}}\left(\beta_{1,l}r_1\right)}{K_{\frac{m}{\upsilon}}\left(\beta_{1,l}R_1\right)}\right)\cos\left[\beta_{1,l}\left(z+h_1\right)\right]\right]\cos\left(\frac{m\left(\theta_1-\gamma\right)}{\upsilon}\right), \tag{17}$$

where

$$F_{m,0}^{(\chi)}\left(r_1\right)=\begin{cases} C_{m,0}^{(\chi)}+D_{m,0}^{(\chi)}\left[1+\ln\left(\frac{r_1}{R_1}\right)\right], & m=0 \\ C_{m,0}^{(\chi)}\left(\frac{r_1}{R_1}\right)^{\left|\frac{m}{\upsilon}\right|}+D_{m,0}^{(\chi)}\left(\frac{r_1}{R_1}\right)^{-\left|\frac{m}{\upsilon}\right|}, & m\neq 0 \end{cases}, \tag{18}$$

in which $C_{m,l}^{(\chi)}$ and $D_{m,l}^{(\chi)}$ are the unknown coefficients to be solved; K_m is the modified Bessel function of the second kind and order m; $\beta_{1,l}$ is the l-th eigenvalue which is given by

$$\beta_{1,l}=\frac{l\pi}{h_1-d_1},\ l=0, 1, 2, 3\ \ldots \tag{19}$$

III, region under the OB:

$$\Phi_\chi^{\mathrm{OB}}\left(r_2,\theta_2,z\right)=\sum_{m=-\infty}^{\infty}\left[B_{m,0}^{(\chi)}\left(\frac{r_2}{R_2}\right)^{|m|}+\sum_{l=1}^{\infty}B_{m,l}^{(\chi)}\frac{I_m\left(\beta_{2,l}r_2\right)}{I_m\left(\beta_{2,l}R_2\right)}\cos\left[\beta_{2,l}\left(z+h_2\right)\right]\right]\mathrm{e}^{\mathrm{i}m\theta_2}+\Phi_{\chi,\mathrm{p}}^{\mathrm{OB}}, \tag{20}$$

where

$$\Phi_{\chi,\mathrm{p}}^{\mathrm{OB}}=\begin{cases}-\Phi_1, & \chi=0\\ 0, & \chi=1,2\\ \dfrac{1}{4\left(h-d_2\right)}\left[2\left(z+h\right)^2-r_2^2\right], & \chi=3\\ \dfrac{\cos\theta_2}{8\left(h-d_2\right)}\left[r_2^3-4r_2\left(z+h\right)^2\right], & \chi=4\end{cases}, \tag{21}$$

in which $B_{m,l}^{(\chi)}$ are the unknown coefficients to be solved; K_m is the modified Bessel function of the second kind; $h_2=h$; $\beta_{2,l}$ is the l-th eigenvalue, which is given by

$$\beta_{2,l}=\frac{l\pi}{h-d_2},\ l=0,\ 1,\ 2,\ 3\ldots \tag{22}$$

IV, outer region:

$$\begin{aligned}\Phi_{\chi}^{\mathrm{out}}\left(r_n,\theta_n,z\right)&=\delta_{\chi,0}\Phi_1+\sum_{m=-\infty}^{\infty}\sum_{l=0}^{\infty}E_{m,l}^{\chi,n}\frac{\tilde{K}_m\left(k_l r_n\right)}{\tilde{K}_m\left(k_l R_n\right)}Z_l\left(z\right)\mathrm{e}^{\mathrm{i}m\theta_n}\\&+\sum_{\substack{j=1\\ j\neq n}}^{2}\sum_{m=-\infty}^{\infty}\sum_{l=0}^{\infty}\frac{E_{m,l}^{\chi,j}Z_l\left(z\right)}{\tilde{K}_m\left(k_l R_j\right)}\sum_{m'=-\infty}^{\infty}\tilde{K}_{m-m'}\left(k_l D\right)\tilde{I}_{-m'}\left(k_l r_n\right)\mathrm{e}^{\mathrm{i}\left(m\alpha_{jn}-m'\alpha_{nj}\right)}\mathrm{e}^{\mathrm{i}m'\theta_n}\end{aligned},\ r_n<D \tag{23}$$

in which $E_{m,l}^{\chi,j}$ are the unknown coefficients to be determined, $\alpha_{1,2}=0$, and $\alpha_{2,1}=\pi$. Following Zheng et al. [62], Φ_{I} in different local cylindrical coordinate systems can be expressed as

$$\Phi_{\mathrm{I}}\left(r_n,\theta_n,z\right)=-\frac{\mathrm{i}gA}{\omega}\frac{Z_0\left(z\right)}{Z_0\left(0\right)}\mathrm{e}^{\mathrm{i}k\delta_{2,n}D\cos\beta}\sum_{m=-\infty}^{\infty}\mathrm{i}^m\mathrm{e}^{-\mathrm{i}m\beta}J_m\left(k_0 r_n\right)\mathrm{e}^{\mathrm{i}m\theta_n}. \tag{24}$$

$$\tilde{K}_m\left(k_l r_n\right)=\begin{cases}H_m\left(k_l r_n\right), & l=0\\ K_m\left(k_l r_n\right), & l\neq 0\end{cases}, \tag{25}$$

where H_m denotes the Hankel function of the first kind and order m.

2.3 Method of computation for unknown coefficients

The scattering/radiated potentials should satisfy the continuity of normal velocity and pressure at the boundaries $r_1=R_{\mathrm{i}}$ and R_1 and $r_2=R_2$, which are given in terms of continuity equations as follows:

1) Continuity of normal velocity at the boundary $r_1=R_{\mathrm{i}}$:

$$\frac{\partial\Phi_{\chi}^{\mathrm{in}}}{\partial r_1}=\begin{cases}0, & z\in[-d_1,0]\cup[-h,-h_1],r_1=R_{\mathrm{i}},\theta_1\in[0,2\pi];\\ & \text{and } z\in[-h_1,-d_1],r_1=R_{\mathrm{i}},\theta_1\notin[\gamma,\gamma+\upsilon\pi]\\ \dfrac{\partial\Phi_{\chi}^{\mathrm{open}}}{\partial r_1}, & z\in[-h_1,-d_1],r_1=R_{\mathrm{i}},\theta_1\in[\gamma,\gamma+\upsilon\pi]\end{cases}, \tag{26}$$

2) Continuity of normal velocity at the boundary r_1=R_1:

$$\frac{\partial \Phi_\chi^{\text{out}}}{\partial r_1}=\begin{cases}0, \quad z\in[-d_1,0]\cup[-h,-h_1], r_1=R_1, \theta_1\in[0,2\pi]; \\ \quad \text{and } z\in[-h_1,-d_1], r_1=R_1, \theta_1\notin[\gamma,\gamma+\upsilon\pi] \\ \dfrac{\partial \Phi_\chi^{\text{open}}}{\partial r_1}, \quad z\in[-h_1,-d_1], r_1=R_1, \theta_1\in[\gamma,\gamma+\upsilon\pi]\end{cases}, \tag{27}$$

3) Continuity of normal velocity at the boundary r_2=R_2:

$$\frac{\partial \Phi_\chi^{\text{out}}}{\partial r_2}=\begin{cases}\delta_{\chi,2}\cos\theta_2+\delta_{\chi,4}\left(z-z_0\right)\cos\theta_2, \quad z\in[-d_2,0], r_2=R_2, \theta_2\in[0,2\pi]; \\ \dfrac{\partial \Phi_\chi^{\text{OB}}}{\partial r_2}, \quad z\in[-h,-d_2], r_2=R_2, \theta_2\in[0,2\pi]\end{cases}, \tag{28}$$

4) Continuity of pressure at the boundary r_1=R_{i}:

$$\Phi_\chi^{\text{open}}=\Phi_\chi^{\text{in}}, \quad z\in[-h_1,-d_1], r_1=R_{\text{i}}, \theta_1\in[\gamma,\gamma+\upsilon\pi], \tag{29}$$

5) Continuity of pressure at the boundary r_1=R_1:

$$\Phi_\chi^{\text{out}}=\Phi_\chi^{\text{open}}, \quad z\in[-h_1,-d_1], r_1=R_1, \theta_1\in[\gamma,\gamma+\upsilon\pi], \tag{30}$$

6) Continuity of pressure at the boundary r_2=R_2:

$$\Phi_\chi^{\text{out}}=\Phi_\chi^{\text{OB}}, \quad z\in[-h,-d_2], r_2=R_2, \theta_2\in[0,2\pi]. \tag{31}$$

After inserting the expressions of the scattering/radiated potentials in different regions as given in Section 2.2 into these continuity equations and using the orthogonal properties of the $Z_l(z)$ and trigonometric functions, the unknown coefficients of the scattering/radiated potentials can be determined. A detailed derivation is given in Appendix A.

2.4 Wave excitation volume flux/forces

The wave excitation volume flux, i.e., the upward flux at the water surface inside the OWC chamber when the dynamic air pressure is zero, can be written as $\text{Re}\left[F_{\text{e}}^{(1)}\text{e}^{-\text{i}\omega t}\right]$. Considering the undisturbed incident wave and the diffracted wave, and using Eq. (12), $F_{\text{e}}^{(1)}$ can be expressed by

$$\begin{aligned}F_{\text{e}}^{(1)}&=\int_0^{2\pi}\int_0^{R_{\text{i}}}\left.\frac{\partial \Phi_0}{\partial z}\right|_{z=0} r_1\text{d}r_1\text{d}\theta_1=\frac{\omega^2}{g}\int_0^{2\pi}\int_0^{R_{\text{i}}}\Phi_0\big|_{z=0}\, r_1\text{d}r_1\text{d}\theta_1 \\ &=\frac{2\pi\omega^2 R_{\text{i}}}{g}\left(-\frac{A_{0,0}^{(0)}}{k_0^2}Z_0\left(0\right)+\sum_{l=1}^{\infty}\frac{A_{0,l}^{(0)}}{k_l^2}Z_l\left(0\right)\right)\end{aligned}. \tag{32}$$

The excitation force/moment acting on the OB in the mode of j (j=2,3,4) is $\text{Re}\left[F_{\text{e}}^{(j)}\text{e}^{-\text{i}\omega t}\right]$, where

$$F_{\text{e}}^{(j)}=-\text{i}\omega\rho\int_S \Phi_0 n_j\text{d}s, \tag{33}$$

in which S is the wetted surface of the OB; n_2=n_x, n_3=n_z, n_4=(z-z_0)n_x-xn_z, where $\vec{n}=n_x\vec{i}+n_y\vec{j}+n_z\vec{k}$ is the unit normal vector pointing into the fluid domain at the wetted surface of the OB. After inserting the analytical expressions for the scattering potential as derived in Section 2.2 into Eq. (33), the wave excitation force acting on the OB in different modes can be calculated directly.

2.5 Hydrodynamic coefficients

When the water column inside the OWC chamber or the OB oscillates in the absence of an incident wave, the radiated wave reacts with an upward flux at the water surface inside the OWC chamber (the so-called radiation volume flux) and force/moment on the OB (the so-called radiation force/moment). The complex amplitudes of the radiation volume flux due to a unit dynamic air pressure inside the OWC chamber (j=1) or a unit amplitude velocity oscillation of the OB oscillating in Mode j (j=2,3,4) can be written into imaginary and real parts as:

$$\begin{aligned} F_{\mathrm{R},j}^{(1)} &= \int_0^{2\pi}\int_0^{R_1} \left.\frac{\partial \Phi_j}{\partial z}\right|_{z=0} r_1 \mathrm{d}r_1 \mathrm{d}\theta_1 \\ &= \frac{2\pi\omega^2 R_1}{g}\left(-\frac{A_{0,0}^{(j)}}{k_0^2}Z_0(0)+\sum_{l=1}^{\infty}\frac{A_{0,l}^{(j)}}{k_l^2}Z_l(0)\right) = \mathrm{i}\omega a_{1,j} - c_{1,j} \end{aligned} . \tag{34}$$

Similarly, the complex amplitudes of the radiation force/moment acting on the OB in Mode j' due to a unit dynamic air pressure inside the OWC chamber (j=1) or a unit amplitude velocity oscillation of OB oscillating in Mode j (j=2,3,4) can be written in terms of hydrodynamic coefficients $a_{j',j}$ and $c_{j',j}$ as:

$$F_{\mathrm{R},j}^{(j')} = -\mathrm{i}\omega\rho\int_S \Phi^{(j)} n_{j'} \mathrm{d}s = \mathrm{i}\omega a_{j',j} - c_{j',j} . \tag{35}$$

The hydrodynamic coefficients $a_{j',j}$ and $c_{j',j}$ (j, j'=1, 2, 3, 4) as obtained from Eqs. (34) and (35) are real and dependent on frequency ω, and represent the hydrodynamic coupling between the OWC and the motion of the OB.

2.6 Motion response and wave power extraction in regular waves

Assuming that both the pneumatic and hydraulic PTO systems are linear, the response of the OWCOB in the frequency domain can be evaluated by solving the following motion response matrix equation:

$$\begin{bmatrix} -\mathrm{i}\omega\left(\mathbf{M}+\mathbf{M}_{\mathrm{a}}+\mathbf{M}_{\mathrm{PTO}}\right)+\left(\mathbf{C}_{\mathrm{d}}+\mathbf{C}_{\mathrm{PTO}}\right)+\mathrm{i}\mathbf{K}_{\mathrm{s}}/\omega & \mathbf{A}_{\mathrm{J}}^{\mathrm{T}} \\ \mathbf{A}_{\mathrm{J}} & \mathbf{0} \end{bmatrix} \begin{Bmatrix} \dot{\boldsymbol{X}} \\ \boldsymbol{F}_{\mathrm{J}} \end{Bmatrix} = \begin{Bmatrix} \boldsymbol{F}_{\mathrm{e}} \\ \mathbf{0} \end{Bmatrix}, \tag{36}$$

where $\mathbf{M}$ and $\mathbf{K}_{\mathrm{s}}$ represent the mass and hydrostatic restoring matrices, respectively; $\mathbf{M}_{\mathrm{a}}$ and $\mathbf{C}_{\mathrm{d}}$ are the hydrodynamic coefficient matrices that are composed of $a_{j',j}$ and $c_{j',j}$, respectively; $\mathbf{M}_{\mathrm{PTO}}$ is the matrix accounting for the influence of air compressibility; $\mathbf{C}_{\mathrm{PTO}}$ is the damping matrix induced by the pneumatic and hydraulic PTO systems; $\mathbf{A}_{\mathrm{J}}$ denotes a constraint matrix due to the hinge restriction; $\dot{\boldsymbol{X}} = [\dot{X}_1, \dot{X}_2, \dot{X}_3, \dot{X}_4]^{\mathrm{T}}$ is the velocity response vector of the OWCOB to be determined; $\boldsymbol{F}_{\mathrm{J}}$ is the hinge force vector; and $\boldsymbol{F}_{\mathrm{e}}$ is the wave excitation volume flux/forces vector. The elements of $\boldsymbol{F}_{\mathrm{e}}$, $\mathbf{M}_{\mathrm{a}}$ and $\mathbf{C}_{\mathrm{d}}$ can be obtained from Sections 2.4 and 2.5. Expressions of $\mathbf{M}_{\mathrm{PTO}}$, $\mathbf{C}_{\mathrm{PTO}}$ and $\mathbf{A}_{\mathrm{J}}$ are as follows:

$$\mathbf{M}_{\mathrm{PTO}} = \begin{bmatrix} \dfrac{\pi R_1^2 h}{c_{\mathrm{a}}^2 \rho_0} & & & \\ & 0 & & \\ & & 0 & \\ & & & 0 \end{bmatrix}, \quad \mathbf{C}_{\mathrm{PTO}} = \begin{bmatrix} c_1 & & & \\ & 0 & & \\ & & 0 & \\ & & & c_2 \end{bmatrix}, \quad \mathbf{A}_{\mathrm{J}} = \begin{bmatrix} 0 & 1 & 0 & d \\ 0 & 0 & 1 & D-R_1 \end{bmatrix}, \tag{37}$$

where c_{a} is the sound velocity in the air; ρ_0 denotes the static air density. In this study, $\rho/\rho_0 = 1000$ and $c_{\mathrm{a}} = 340$ m/s are adopted. c_1 and c_2 are the PTO damping coefficients of the pneumatic and

hydraulic PTO systems selected to maximize power absorption of the OWCOB, which can be obtained by using an analytical model derived by Zheng and Zhang [60].

After solving the response of the OWCOB, the time-averaged power that is captured from regular waves can be evaluated by

$$P=\frac{1}{2}\left(c_1\left|\dot{X}_1\right|^2+c_2\left|\dot{X}_4\right|^2\right), \tag{38}$$

which can be further expressed by a nondimensionalized parameter, i.e., the power capture factor,

$$\eta=\frac{2Pk}{\rho g A^2 c_g}, \tag{39}$$

where k is employed hereinafter to represent k_0 for simplicity, and c_g is the group velocity.

2.7 Wave power extraction in irregular waves

The JONSWAP spectrum was used to describe the incident wave field, and from this the wave power absorption of the OWCOB in irregular waves was evaluated. The JONSWAP spectrum can be expressed as [63]

$$S_\xi\left(\omega_p,\omega\right)=\frac{\alpha_\xi H_s^2}{\omega}\left(\frac{\omega_p}{\omega}\right)^4 \mathrm{e}^{-1.25\left(\omega_p/\omega\right)^4}\gamma_\xi^{\exp\left[-\left(\omega/\omega_p-1\right)^2/\left(2\sigma^2\right)\right]}, \tag{40}$$

where H_s is the significant wave height, ω_p is the peak frequency, and

$$\alpha_\xi=\frac{0.0624\left(1.094-0.01915\ln\gamma_\xi\right)}{0.23+0.0336\gamma_\xi-0.185\left(1.9+\gamma_\xi\right)^{-1}},\quad \sigma=\begin{cases}0.07, & \omega\le\omega_p\\ 0.09, & \omega>\omega_p\end{cases},\quad \gamma_\xi=3.3. \tag{41}$$

The time-averaged wave power absorption in irregular waves may be calculated by

$$P_{irr}\left(\omega_p\right)=\int_0^\infty S_\xi\left(\omega_p,\omega\right)\left(c_1^*\left|\dot{X}_1^*\left(\omega\right)\right|^2+c_2^*\left|\dot{X}_4^*\left(\omega\right)\right|^2\right)\mathrm{d}\omega, \tag{42}$$

where c_1^* and c_2^* are two frequency-independent PTO damping coefficients different from c_1 and c_2, the frequency-dependent optimized PTO damping coefficients; and $\dot{X}_1^*$ and $\dot{X}_4^*$ are the modified $\dot{X}_1$ and $\dot{X}_4$, which can be calculated with Eq. (36) if c_1 and c_2 are replaced by c_1^* and c_2^*, respectively, based on a regular wave with an amplitude of 1 m (A = 1.0 m).

The total incident wave power of the irregular waves per unit crest width is

$$P_{in,irr}\left(\omega_p\right)=\int_0^\infty \rho g c_g\left(\omega\right)S_\xi\left(\omega_p,\omega\right)\mathrm{d}\omega. \tag{43}$$

The power capture factor in irregular waves η_{irr}^* can then be written as

$$\eta_{irr}^*=\frac{k^*P_{irr}}{P_{in,irr}}, \tag{44}$$

in which k^* satisfies $\omega_p^2=gk^*\tanh\left(k^*h\right)$.

Similarly, the power capture factor in regular waves is rewritten as:

$$\eta^* = \frac{2kP^*}{\rho g A^2 c_g}, \tag{45}$$

where P^* is a modified P, which can be calculated with the employment of Eqs. (36) and (38) as well but with c_1 and c_2 replaced by c_1^* and c_2^*, respectively.

3 Validation

For the device with $\alpha=2\pi$, i.e., $\upsilon=2$, and subjected to incident waves with either $\beta=0$ or π, the wave diffraction and radiation problems become the same as those for a hollow cylinder and a solid cylinder, which can be solved with the analytical model of Zheng et al. [62]. When $D\to\infty$, the device transforms itself into an isolated OWC and an isolated buoy [64], with negligible hydrodynamic interaction between the two. For $R_i\to R_1$ and $h_1=h$, i.e., $d_1+d_0=h$, the isolated OWC behaviour is described by Deng et al. [46]. These two extreme cases – Case I, a hollow cylinder and a solid cylinder [62], and Case II, an isolated OWC [46] and an isolated buoy [64] – may be used to validate the present analytical model.

The dimensionless wave diffraction and radiation-related parameters are chosen as follows unless defined otherwise:

$$\bar{F}_{\mathrm{e}}^{(1)} = \frac{\sqrt{g/h}}{Ahg} F_{\mathrm{e}}^{(1)}, \quad \left(\bar{c}_{1,1}, \bar{a}_{1,1}, \bar{c}_{\mathrm{PTO}}^{(1)}, \bar{a}_{\mathrm{PTO}}^{(1)}\right) = \frac{\rho\sqrt{g/h}}{h}\left(c_{1,1}, \omega a_{1,1}, c_{\mathrm{PTO}}^{(1)}, \omega a_{\mathrm{PTO}}^{(1)}\right) \tag{46a}$$

$$\bar{F}_{\mathrm{e}}^{(4)} = \frac{1}{\rho g h^3 A} F_{\mathrm{e}}^{(4)}, \quad \left(\bar{c}_{4,4}, \bar{a}_{4,4}, \bar{c}_{\mathrm{PTO}}^{(2)}, \bar{a}_{\mathrm{PTO}}^{(2)}\right) = \frac{1}{\rho h^4\sqrt{gh}}\left(c_{4,4}, \omega a_{4,4}, c_{\mathrm{PTO}}^{(2)}, \omega a_{\mathrm{PTO}}^{(2)}\right) \tag{46b}$$

$$\bar{F}_{\mathrm{e}}^{(j)} = \frac{1}{\rho g h^2 A} F_{\mathrm{e}}^{(j)}, \quad \left(\bar{c}_{j,j'}, \bar{a}_{j,j'}\right) = \frac{1}{\rho h^2\sqrt{gh}}\left(c_{j,j'}, \omega a_{j,j'}\right), \text{ for } j, j'=2,3 \tag{46c}$$

$$\left(\bar{c}_{j,j'}, \bar{a}_{j,j'}\right) = \frac{1}{h^2}\left(c_{j,j'}, \omega a_{j,j'}\right), \text{ for } j=1, j'=2,3; \text{ or } j=2,3, j'=1 \tag{46d}$$

$$\left(\bar{c}_{j,j'}, \bar{a}_{j,j'}\right) = \frac{1}{h^3}\left(c_{j,j'}, \omega a_{j,j'}\right), \text{ for } j=1, j'=4; \text{ or } j=4, j'=1 \tag{46e}$$

$$\left(\bar{c}_{j,j'}, \bar{a}_{j,j'}\right) = \frac{1}{\rho h^3\sqrt{gh}}\left(c_{j,j'}, \omega a_{j,j'}\right), \text{ for } j=2,3, j'=4; \text{ or } j=4, j'=2,3 \tag{46f}$$

Figures 2 and 3 present the comparison of the dimensionless wave excitation flux/forces and hydrodynamic coefficients calculated with the present and previous models [46, 62, 64] for Cases I and II, respectively. In Case II, $(R_1-R_i)/h=0.01$ and $D/h=100$ are adopted to approximately match the thin-walled assumption as employed by Deng et al. [46] and to minimize the hydrodynamic interaction between the OWC and the OB, respectively.

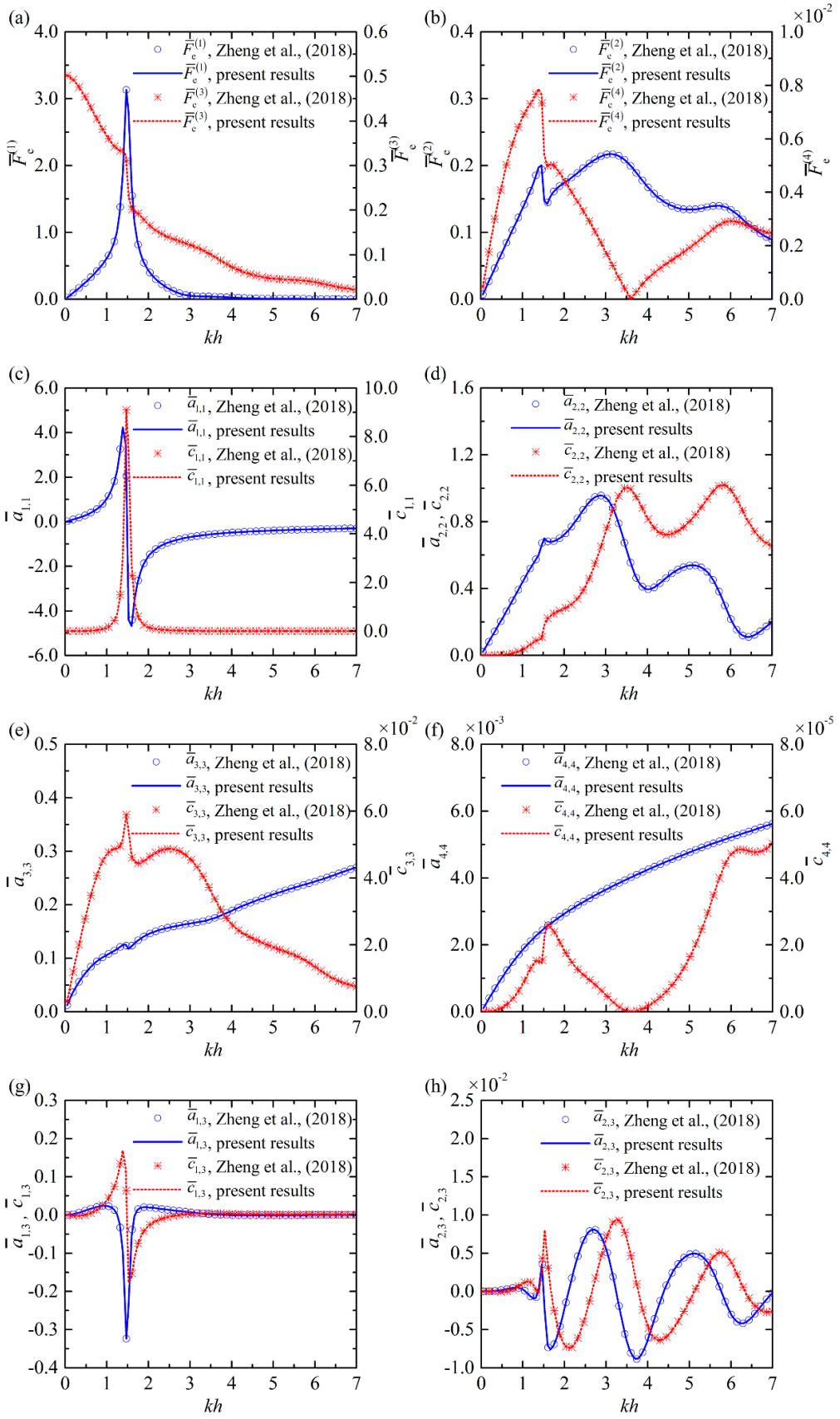


Fig. 2. Comparison using dimensionless hydrodynamic parameters between the present analytical model and the model by Zheng et al. [62] for Case I, i.e., a hollow cylinder and a solid

cylinder [R_1/h=0.5, R_i/h=0.4, α=2.0π, γ=0, d_0/h=0.5, d_1/h=0.5, R_2/h=0.4, d_2/h=0.2, D/h=2.0, β=0].

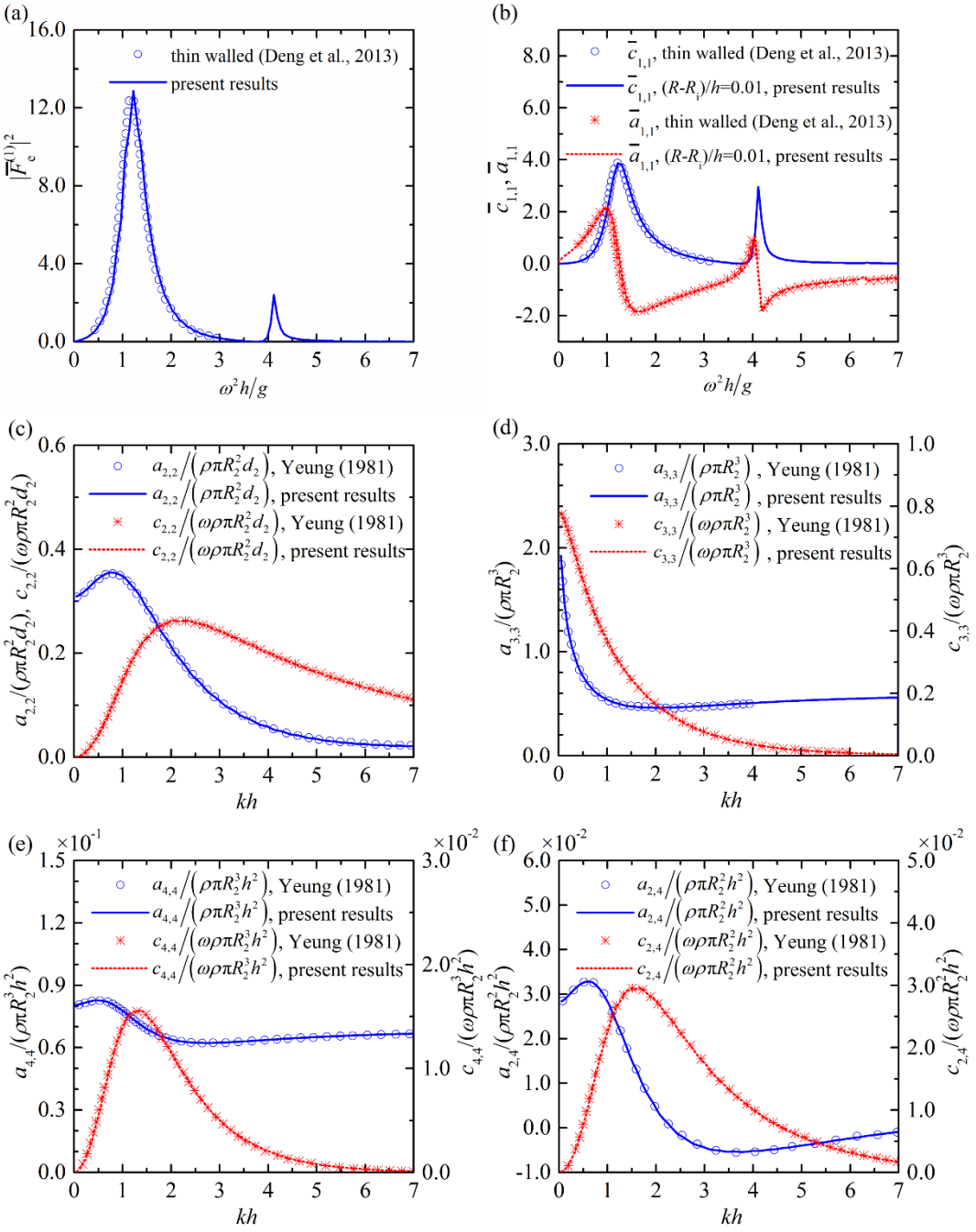


Fig. 3. Comparison using dimensionless hydrodynamic parameters between the present analytical model and the models by Deng et al. [46] and Yeung [64] for Case II, i.e., an isolated OWC and an isolated buoy [R_1/h=0.5, R_i/h=0.49, α=0.75π, γ=π, d_0/h=0.8, d_1/h=0.2, R_2/h=1.0, d_2/h=0.25, D/h=100, β=0.5α]

The excellent agreement between the results of the present and previous model is apparent in Figs. 2 and 3, and the model output is analysed further on this basis. It is worth noting that the model presented here was developed using linear potential flow theory, and therefore did not capture viscous effects. While these may be important in extreme wave conditions, the linear model is useful

in quantifying OWCOB performance in the more usual range of non-extreme sea states.

4 Results and discussion

The model was run in a variety of scenarios. The OWCOB was initially compared to the isolated OWC and OB cases. The model was then applied to investigate the effects of: incident wave direction; OWC opening size; OWC opening submergence; distance between OWC and OB; hinge position; and OB radius. Finally the power absorption in regular and irregular waves was investigated.

4.1 Comparison between OWCOB and isolated OWC and OB

In this subsection, wave power extraction by the OWCOB is compared with stand-alone OWC [65] and OB working in isolation (Fig. 4), i.e., an OWC and an OB hinged on a leg standing on the seabed, respectively, working in the open sea.

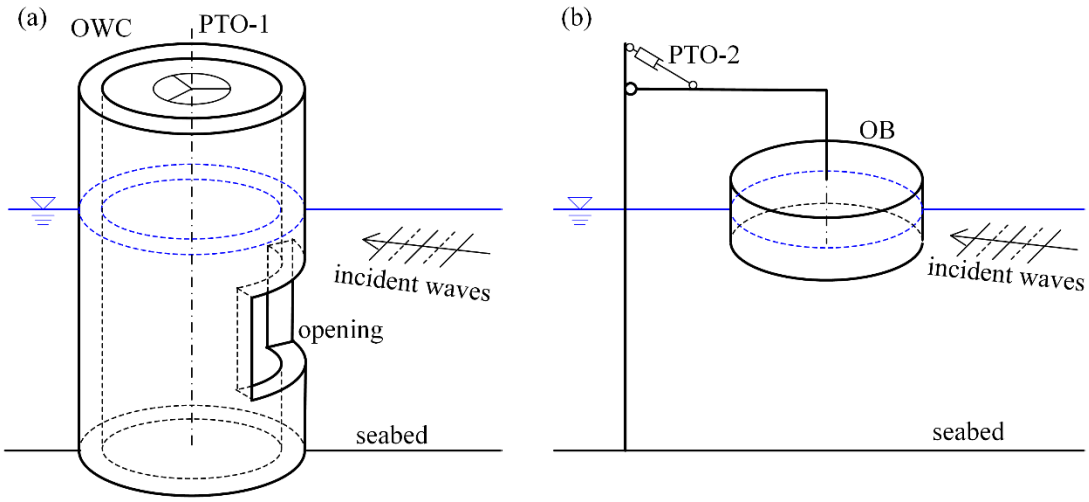


Fig. 4. Sketch of the individual (a) OWC and (b) OB working in isolation

Two cases are considered (Fig. 5): in case 1, the OB is articulated on the same side of the OWC opening (i.e., $\gamma+\alpha/2=0$); in case 2, the OB is articulated on the opposite side of the OWC (i.e., $\gamma+\alpha/2=\pi$).

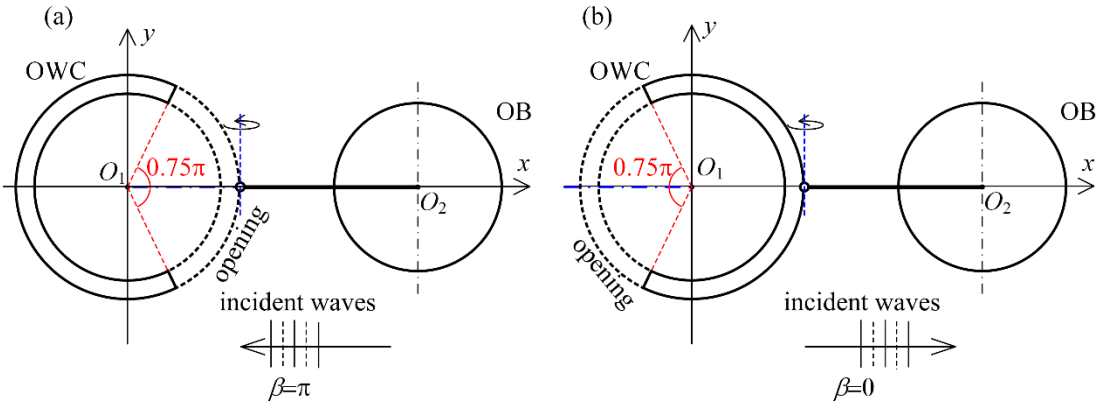


Fig. 5. Two configurations of OWCOB: (a) case 1, OB on the side of the OWC opening, $\gamma+\alpha/2=0$; (b) case 2, OB on the opposite side of the OWC, $\gamma+\alpha/2=\pi$. [$R_1/h=0.5$, $R_i/h=0.4$, $\alpha=0.75\pi$, $d_0/h=0.3$, $d_1/h=0.2$, $R_2/h=0.4$, $d_2/h=0.2$, $D/h=1.5$, $d/h=0.5$]

Figure 6 presents the performance comparison between the OWCOB and the isolated OWC and OB for cases 1 and 2, in which η_{OWC} and η_{OB} denote the power capture factor of the isolated OWC and OB with the corresponding PTO damping optimized, respectively. Importantly, the OWCOB is advantageous in terms of frequency bandwidth (see Fig. 6a) and incident wave direction bandwidth (see Fig. 6b) relative to stand-alone OWCs or OBs. This holds for both configurations, case 1 and 2.

As expected, the η_{OWC}-kh curves for cases 1 and 2 overlap each other (Fig. 6a). The isolated OB with incident waves from the hinge side (i.e., the isolated OB for case 2) performs much better than in case 1 in terms of both peak power absorption and frequency bandwidth of high efficiency (large power capture), indicating the considerable influence of the hinge position (or incident wave direction) on wave power extraction. Indeed, the coupling between the surge, heave and pitch modes of the OB motion is strongly influenced by the hinge position.The peak value of η occurring around kh=2.0 in case 1 (η=3.98) is larger than in case 2 (η=3.26), which may be induced by a constructive hydrodynamic interaction between the OWC and the OB. However, the overall performance of OWCOB in case 2 is drastically better than in case 1, especially for higher frequencies, kh>2.1. The main bandwidths of η>2.0 for cases 1 and 2 are 0.98 and 1.54, respectively. A sharp peak of the η-kh curve for both cases at $kh\approx4.8$ results from the strong response of the OWC – a sharp peak is also apparent on the η_{OWC}-kh curve at the same frequency, but not on the η_{OB}-kh curve. The sharp peak of η for case 2 is slightly higher and broader than that of η_{OWC}, whereas for case 1 the sharp peak of η is slightly lower and narrower compared with that of η_{OWC}.

The variation of η, η_{OWC}, and η_{OB} versus the incident wave direction, β, for kh=2.0 is plotted in Fig. 6b. The largest value of η_{OWC} is observed when the OWC opening is on the waveward side with its axis of symmetry exactly perpendicular to the wavefront, which agrees well with the results of Deng et al. [46]. The η_{OB}-β curves for cases 1 and 2 overlap each other as expected. The main peak value of η and the corresponding β are (3.9, π) and (3.3, 0) for cases 1 and 2, respectively. By contrast, when the incident wave direction is 0.2π away from its optimum, the η-value reduces to 2.2 in case 1, but remains above 2.4 in case 2. From a practical point of view this is an important result – it means that the configuration of case 2 can capture significant power from a larger range of incident wave directions.

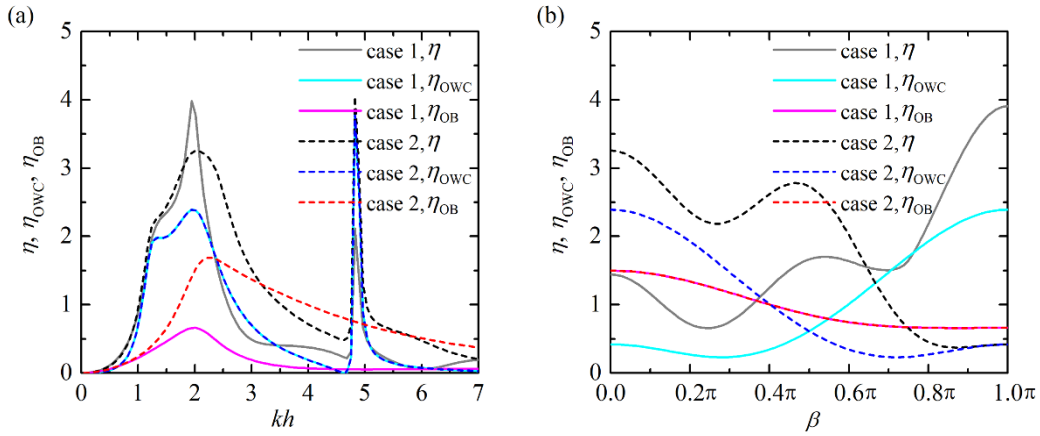


Fig. 6. (a) Variation of η, η_{OWC}, η_{OB} with kh for case 1 with β=π and case 2 with β=0; (b) Variation of η, η_{OWC}, η_{OB} with β for cases 1 and 2, kh=2.0.

Notice that in Fig. 6b, as β varies from 0 to π for kh=2.0, η basically oscillates around 2.0. In fact, for any given wave frequency, there is a general identity that the integral of the optimum wave capture factor (η_{MAX}) over all incidence angles must satisfy regardless of the dimensions of the OWCOB:

$$\frac{1}{2\pi}\int_0^{2\pi}\eta_{MAX}(\beta)\,\mathrm{d}\beta = 2\,. \tag{47}$$

This can be theoretically confirmed by invoking the ideal optimization criteria and the Haskind relation. A detailed derivation is given in Appendix B.

As may be readily seen in Fig. 6, the OWCOB in case 2 works better than in case 1 from the point of view of the bandwidth of high wave power capture factor, both in terms of frequency response and incident wave direction response for kh=2.0. For this reason, the following multi-parameter sensitivity analysis is focused on the case 2 configuration, i.e., with the OWC opening and the OB on the waveward and leeward sides of the OWC, respectively (Fig. 6b).

4.2 Effect of incident wave direction

Figure 7 presents the frequency responses of η when a monochromatic plane wave is incoming from different directions, i.e., β=0, 0.25π, 0.5π, 0.75π, 1.0π. For 1.0<kh<4.0, the power captured by the OWCOB with β=0 is the largest among the five cases. What is more, the corresponding bandwidth of high wave power capture factor is the largest as well. Specifically, the peak value of η and the η>2.0 bandwidth for β=0, 0.25π, 0.5π are (3.26, 1.51), (2.22, 0.63) and (2.93, 0.70), respectively. For short waves, e.g., kh>5.0, the OWCOB with β=0.25π is observed to absorb more power than the other four cases. When the incident waves propagate perpendicular to the axis of symmetry of the OWCOB, i.e., β= 0.5π, a sharp peak of η around kh=2.2 is obtained, whereas the overall wave power absorption for 4.0<kh<7.0 is the worst. When β increases to 0.5π and 0.75π, the main peak of η shifts towards low wave frequencies (kh≈1.2) with the peak value dropping drastically to 1.21~1.28.

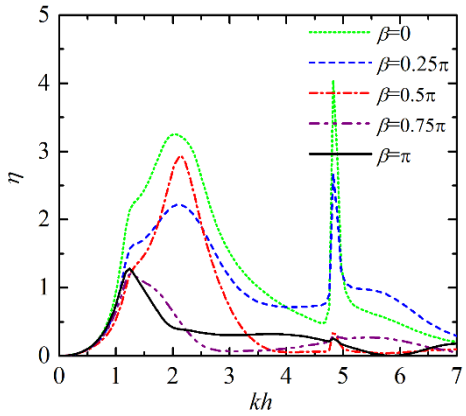


Fig. 7. Variation of η with kh for β=0, 0.25π, 0.5π, 0.75π, 1.0π. [R_1/h=0.5, R_i/h=0.4, α=0.75π, $\gamma+\alpha/2$=π, d_0/h=0.3, d_1/h=0.2, R_2/h=0.4, d_2/h=0.2, D/h=1.5, d/h=0.5]

4.3 Effect of OWC opening size

The opening size of the OWC is a key factor affecting the power extraction of OWCOB. The frequency responses of η for the device with opening sizes α=0.5π, 0.625π, 0.75π, 0.875π, 1.0 are plotted in Fig. 8. As α increases from 0.5π to 1.0π, the main peak of η rises linearly, broadens, and shifts towards higher frequencies. This can be explained by resonance in the OWC chamber: when the opening grows in size, the mass of the water column restricted by the OWC chamber decreases, leading to higher resonant frequencies, which in turn results in the peak of η shifting towards higher incident wave frequencies.

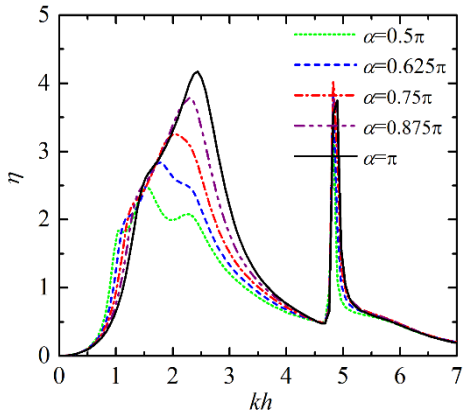


Fig. 8. Variation of η with kh for α=0.5π, 0.625π, 0.75π, 0.875π, 1.0π. [R_1/h=0.5, R_i/h=0.4, $\gamma+\alpha/2$=π, d_0/h=0.3, d_1/h=0.2, R_2/h=0.4, d_2/h=0.2, D/h=1.5, d/h=0.5, β=0]

4.4 Effect of OWC opening submergence

In this subsection the wave power extraction of the OWCOB with different values of the opening submergence, i.e., d_1/h=0.1, 0.15, 0.2, 0.25, 0.3, is examined (Fig. 9). It will be seen that the OWCOB with a smaller submergence of the opening performs better in terms of both the main peak and the frequency bandwidth of wave energy capture. This is reasonable because most wave power (approximately 95%) is concentrated at no more than a quarter of a wavelength below the sea water level [1], and the lower the position below the water level, the weaker the wave power

density. A similar effect of the opening submergence also applies to the sharp peak of η around kh=5.0.

In practice, the submergence of the opening should be large enough to keep the opening continuously submerged, so that air does not escape through it. Needless to say, the tidal range and wave climate at the site of deployment must be taken into account in determining the submergence.

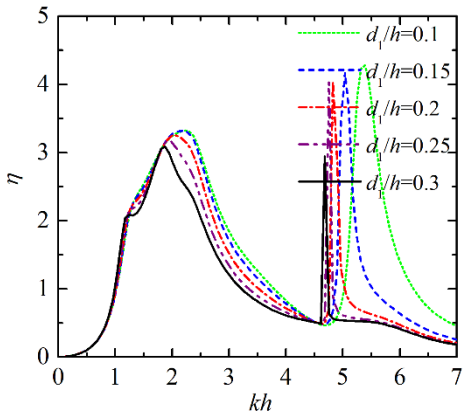


Fig. 9. Variation of η with kh for d_1/h=0.1, 0.15, 0.2, 0.25, 0.3. [R_1/h=0.5, R_i/h=0.4, α=0.75π, $\gamma+\alpha/2=\pi$, d_0/h=0.3, R_2/h=0.4, d_2/h=0.2, D/h=1.5, d/h=0.5, β=0]

4.5 Effect of distance between OWC and OB

The hydrodynamic interaction between the OWC and OB may be expected to vary with the distance D between them. To ascertain this point the performance of the OWCOB for five cases, with D/h=1.2, 1.35, 1.5, 1.65, 1.8, is compared (Fig. 10). Wave power extraction for long waves, e.g., kh<1.2, and around kh=4.8, where the sharp peak occurs, is almost independent of D/h. For the rest of the computed range of kh, η varies to some extent with D/h, reflecting the hydrodynamic interaction between the two subsystems.

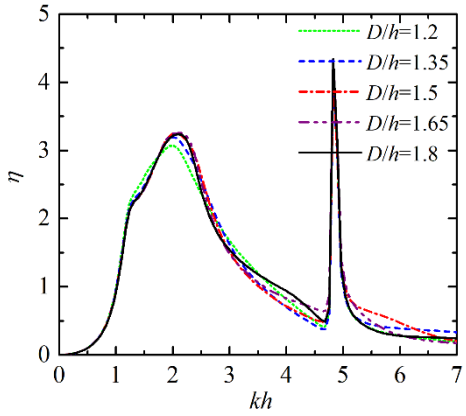


Fig. 10. Variation of η with kh for D/h=1.2, 1.35, 1.5, 1.65, 1.8. [R_1/h=0.5, R_i/h=0.4, α=0.75π, $\gamma+\alpha/2=\pi$, d_0/h=0.3, d_1/h=0.2, R_2/h=0.4, d_2/h=0.2, d/h=0.5, β=0]

4.6 Effect of hinge position

Although the elevation of the hinge (d/h) does not affect the basic wave excitation moment and

hydrodynamic coefficients of the OB relative to its mass centre as calculated in the analytical model, it has a significant influence on the rotary stiffness and inertia of the OB, the wave excitation moment and the rotary hydrodynamic coefficients relative to the hinge point.

In order to study the effect of the vertical position of the hinge on power absorption of the OWCOB, the frequency responses of η for the device with d/h=-0.5, -0.25, 0, 0.25, 0.5 are examined in this subsection (Fig. 11). For relatively long waves, e.g., kh<1.2, the performance of the OWCOB is not significantly influenced by the vertical hinge position. For shorter waves, the wave power absorption of the device becomes more dependent on the value of d/h. Although the largest value of the main peak (η=3.3) is obtained for the device with the lowest hinge position (d/h=-0.5), a significant improvement in η can be achieved for 2.3<kh<7.0 by raising the hinge position. In other words, the highest hinge position of the five considered led to the best results.

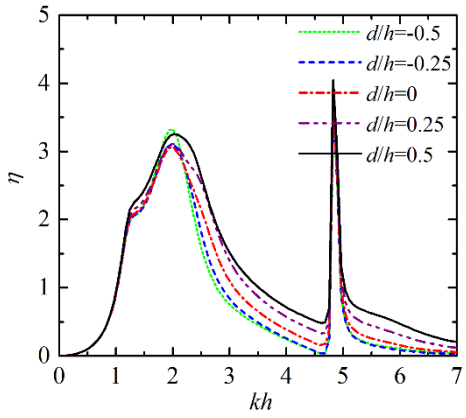


Fig. 11. Variation of η with kh for d/h=-0.5, -0.25, 0, 0.25, 0.5. [R_1/h=0.5, R_i/h=0.4, α=0.75π, $\gamma+\alpha/2$=π, d_0/h=0.3, d_1/h=0.2, R_2/h=0.4, d_2/h=0.2, D/h=1.5, β=0]

4.7 Effect of OB radius

The OB radius also affects the behaviour of the OWCOB. Wave power absorption of the device with different values of the OB radius, i.e., R_2/h=0.3, 0.35, 0.4, 0.45 and 0.5, was examined (Fig. 12).

In the computed range of wave conditions, as R_2/h increases η is found to increase and decrease, respectively, for kh<2.4 and 3.0<kh<6.0. This may be explained from the point of view of the natural frequency of the OB. As R_2/h becomes large, the OB mass grows, leading to a smaller natural frequency of the OB. Therefore, a larger value of R_2/h is generally advantageous for small wave frequencies, e.g., kh<2.4, and in contrast, disadvantageous for large wave frequencies, e.g., 3.0<kh<6.0.

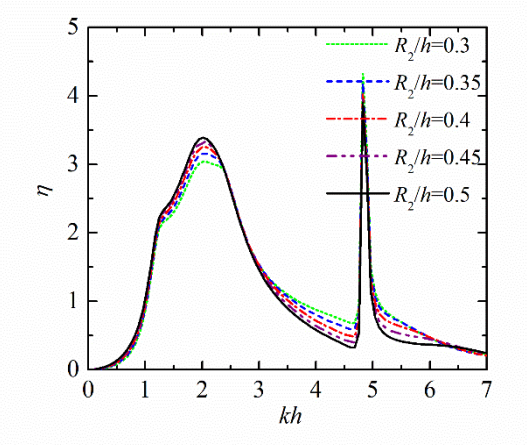


Fig. 12 Variation of η with kh for $R2/h$ =0.3, 0.35, 0.4, 0.45, 0.5. [$R1/h$=0.5, Ri/h=0.4, α=0.75π, $\gamma+\alpha/2$=π, $d0/h$=0.3, $d1/h$ =0.2, $d2/h$=0.2, D/h=1.5, d/h=0.5, β=0]

4.8 Wave power absorption in regular and irregular waves

Let us fix the values of c_1^* and c_2^* that maximise power extraction for specific wave conditions, kh = 2.0. Fixing the optimal values of PTO coefficients that maximise power extraction for a fixed wave condition can be of practical interest due to the difficulty in tuning the pneumatic and hydraulic PTO systems with a wide range of wave frequencies.

Fig. 13 presents the behaviour of η^* and η_{irr}^*, where the abscissa for η_{irr}^* refers to k^*h, which is associated with the peak frequency ω_p of the JONSWAP spectrum, while the abscissa for η^* refers to kh, which is associated with the frequency of the monochromatic incident waves. Unlike the bimodal η^*-kh curve, the η_{irr}^* - k^*h curve is found to be unimodal in the computed range of wave conditions. Both curves peak around kh(k^*h)=2.0. The corresponding peak value of η_{irr}^* is found to be smaller than that of η^*. The narrow peak of the η^*-kh curve occurs around kh=5.0. Although $\eta_{irr}^* < \eta^*$ is observed around the two resonant frequencies ($kh \approx$2.0 and 5.0), the OWCOB in irregular wave conditions becomes more efficient outside the resonant frequencies. Similar results were reported in the context of OWCs [66] and flap-type oscillating wave surge converters [67].

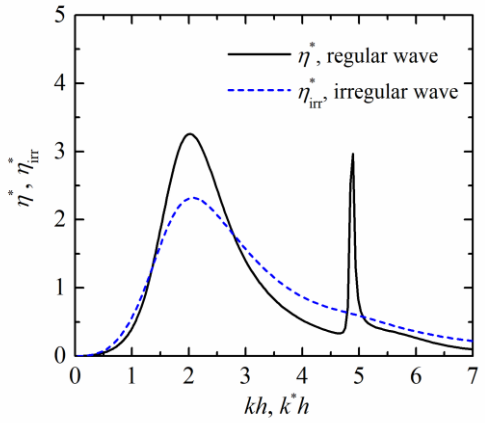


Fig. 13 Variation of η^* (η_{irr}^*) with kh (k^*h) for (c_1^*, c_2^*)=(c_1, c_2)$|_{kh=2.0}$. [$R1/h$=0.5, Ri/h=0.4, α=0.75π, $\gamma+\alpha/2$=π, $d0/h$=0.3, $d1/h$ =0.2, $R2/h$=0.4, $d2/h$=0.2, D/h=1.5, d/h=0.5, β=0]

5 Conclusions

A new, hybrid concept of wave energy converter, referred to as OWCOB, was proposed, which combines an Oscillating Water Column (OWC) and an Oscillating Buoy (OB) hinged on its side. In order to solve the problems of wave diffraction and radiation from the OWCOB, an analytical model based on linear potential flow theory and an eigenfunction matching method was developed. The wave power extraction of the OWCOB was then evaluated considering linear PTOs for both the OWC and OB. The model gave similar output to previous numerical models of OWCs and OBs. The model was then applied to investigate the performance of the hybrid WEC. It was found that the OWCOB performs generally better than stand-alone OWCs or OBs in terms of both frequency bandwidth and incident wave angle bandwidth.

In addition, a multi-parameter sensitivity analysis on the power extraction of the OWCOB was carried out, including the effect of its general configuration (the positions of the OWC opening and the OB relative to the incident wave direction), the incident wave direction, the size and submergence of the OWC opening, the distance between the OWC and the OB, the OB hinge height and the OB radius.

The configuration with the OWC opening waveward and the OB hinge leeward (case 2) was found to be advantageous in terms of wave power absorption; more specifically, it was found to have a broader primary band of power capture factor response compared to the configuration with the OB on the same side as the OWC opening (case 1). The main bandwidths of η>2.0 for cases 1 and 2 are 0.98 and 1.54, respectively. The rest of the multi-parameter study was carried out based on the configuration of case 2. For different incident wave directions with $1.0<kh<4.0$, the power captured by the OWCOB is greatest when the OWC and OB are in line with the wave direction. As the angle of the OWC opening, α, increases from 0.5π to 1.0π, the value of the main peak of the wave power capture factor increases linearly. Meanwhile, the main peak broadens (in terms of frequency response) and its position shifts towards larger wave frequencies. The frequency band of the power capture factor response can be further broadened by decreasing the submergence of the opening and/or increasing the elevation of the hinge. These results indicate the variations in geometry and configuration that can be explored in optimizing the OWCOB design for a specific site, i.e., a specific wave climate.

The findings in this paper are expected to encourage OWC developers to consider the possibility of adding an additional OB to an OWC in order to improve the overall wave power absorption. The OWC in the present OWCOB is placed on a tubular structure, which facilitates its installation on many marine structures – including offshore wind turbines.

It should be noted that combining two separate technologies on the same WEC may increase both building costs (CAPEX) and O&M costs (OPEX) due to the increased overall complexity of the device. In addition to the hydrodynamics and wave power extraction performance of the OWCOB, which are the focus of this work, the Levelised Cost of Energy (LCoE) of the device (including its CAPEX and OPEX) should be carefully evaluated. This evaluation is beyond the scope of this paper and, therefore, left for future work.

Acknowledgements

This research was supported by Intelligent Community Energy (ICE), INTERREG V FCE, European Commission (Contract No. 5025) and the National Natural Science Foundation of China

(51679124, 51879144).

Appendix A. Integral equations of the scattering and radiation problems

1) After inserting Eqs. (12) and (17) into Eq. (26), multiplying both sides by $Z_\zeta(z)\,\mathrm{e}^{-\mathrm{i}\tau\theta_1}$ and integrating for $z\in[-h,0]$ and $\theta_1\in[0,2\pi]$, for any pair of integer (τ, ζ), it can be shown that

$$\upsilon\sum_{l=0}^{\infty}\left[\frac{\pi}{\varepsilon_{|\tau|}}\left(X^{(1)}_{\upsilon|\tau|,l}C^{(\chi)}_{\upsilon|\tau|,l}+Y^{(1)}_{\upsilon|\tau|,l}D^{(\chi)}_{\upsilon|\tau|,l}\right)+\mathrm{i}\sum_{\substack{m=0\\ m\neq\upsilon|\tau|}}^{\infty}\frac{(\upsilon\tau+m)\mathrm{e}^{\mathrm{i}(m-\upsilon\tau)\pi}+(\upsilon\tau-m)\mathrm{e}^{-\mathrm{i}(m+\upsilon\tau)\pi}-2\upsilon\tau}{2\left(\upsilon^2\tau^2-m^2\right)}\left(X^{(1)}_{m,l}C^{(\chi)}_{m,l}+Y^{(1)}_{m,l}D^{(\chi)}_{m,l}\right)\right]L^{(1)}_{l,\zeta}$$
$$-2\pi h\mathrm{e}^{\mathrm{i}\tau\gamma}A^{\chi,1}_{\tau,\zeta}=0 \tag{A.1}$$

where

$$X^{(1)}_{\tau,\zeta}=\begin{cases}\dfrac{\tau}{\upsilon R_1}\left(\dfrac{R_\mathrm{i}}{R_1}\right)^{\frac{\tau}{\upsilon}-1}, & \zeta=0\\ \dfrac{\beta_{1,\zeta}I'_{\frac{\tau}{\upsilon}}\left(\beta_{1,\zeta}R_\mathrm{i}\right)}{I_{\frac{\tau}{\upsilon}}\left(\beta_{1,\zeta}R_1\right)}, & \zeta\neq0\end{cases};\quad Y^{(1)}_{\tau,\zeta}=\begin{cases}\dfrac{1}{R_\mathrm{i}}, & \zeta=0,\tau=0\\ -\dfrac{\tau}{\upsilon R_1}\left(\dfrac{R_1}{R_\mathrm{i}}\right)^{\frac{\tau}{\upsilon}+1}, & \zeta=0,\tau\neq0\\ \dfrac{\beta_{1,\zeta}K'_{\frac{\tau}{\upsilon}}\left(\beta_{1,\zeta}R_\mathrm{i}\right)}{K_{\frac{\tau}{\upsilon}}\left(\beta_{1,\zeta}R_1\right)}, & \zeta\neq0\end{cases}. \tag{A.2}$$

$$\begin{aligned}L^{(n)}_{l,\zeta}&=\int_{-h_n}^{-d_n}\cos\left[\beta_{n,l}\left(z+h_n\right)\right]Z_\zeta\left(z\right)\mathrm{d}z\\ &=\begin{cases}\dfrac{k_0Z_0\left(0\right)\left(h_n-d_n\right)^2\left\{(-1)^l\sinh\left[k_0\left(h-d_n\right)\right]-\sinh\left[k_0\left(h-h_n\right)\right]\right\}}{\left[\left(h_n-d_n\right)^2k_0^2+l^2\pi^2\right]\cosh\left(k_0h\right)}, & \zeta=0\\ \dfrac{k_\zeta Z_\zeta\left(0\right)\left(h_n-d_n\right)^2\left\{(-1)^l\sin\left[k_\zeta\left(h-d_n\right)\right]-\sin\left[k_\zeta\left(h-h_n\right)\right]\right\}}{\left[\left(h_n-d_n\right)^2k_\zeta^2-l^2\pi^2\right]\cos\left(k_\zeta h\right)}, & \zeta\neq0\end{cases}.\end{aligned} \tag{A.3}$$

2) After inserting Eqs. (17) and (23) into Eq. (27), multiplying both sides by $Z_\zeta(z)\,\mathrm{e}^{-\mathrm{i}\tau\theta_1}$ and integrating for $z\in[-h,0]$ and $\theta_1\in[0,2\pi]$, for any pair of integer (τ, ζ), we have

$$\upsilon\sum_{l=0}^{\infty}\left[\frac{\pi}{\varepsilon_{|\tau|}}\left(X^{(2)}_{\upsilon|\tau|,l}C^{(\chi)}_{\upsilon|\tau|,l}+Y^{(2)}_{\upsilon|\tau|,l}D^{(\chi)}_{\upsilon|\tau|,l}\right)+\mathrm{i}\sum_{\substack{m=0\\ m\neq\upsilon|\tau|}}^{\infty}\frac{(\upsilon\tau+m)\mathrm{e}^{\mathrm{i}(m-\upsilon\tau)\pi}+(\upsilon\tau-m)\mathrm{e}^{-\mathrm{i}(m+\upsilon\tau)\pi}-2\upsilon\tau}{2\left(\upsilon^2\tau^2-m^2\right)}\left(X^{(2)}_{m,l}C^{(\chi)}_{m,l}+Y^{(2)}_{m,l}D^{(\chi)}_{m,l}\right)\right]L^{(1)}_{l,\zeta}$$
$$-2\pi h\mathrm{e}^{\mathrm{i}\tau\gamma}\left(\frac{k_\zeta\tilde{K}'_\tau\left(k_\zeta R_1\right)}{\tilde{K}_\tau\left(k_\zeta R_1\right)}E^{\chi,1}_{\tau,\zeta}+\sum_{m=-\infty}^{\infty}T'^{1,2}_{m,\tau,\zeta}E^{\chi,2}_{m,\zeta}\right)=-\frac{2\pi\delta_{\zeta,0}\delta_{\chi,0}\mathrm{i}gAk_0h}{\omega Z_0\left(0\right)}\mathrm{e}^{\mathrm{i}k_0\left(x_1\cos\beta+y_1\sin\beta\right)}\mathrm{i}^\tau J'_\tau\left(k_0R_1\right)\mathrm{e}^{\mathrm{i}\tau\gamma}\mathrm{e}^{-\mathrm{i}\tau\beta} \tag{A.4}$$

in which

$$X_{\tau,\zeta}^{(2)}=\begin{cases}\dfrac{\tau}{\upsilon R_1}, & \zeta=0\\ \dfrac{\beta_{1,\zeta}I'_{\frac{\tau}{\upsilon}}\left(\beta_{1,\zeta}R_1\right)}{I_{\frac{\tau}{\upsilon}}\left(\beta_{1,\zeta}R_1\right)}, & \zeta\neq 0\end{cases};\quad Y_{\tau,\zeta}^{(2)}=\begin{cases}\dfrac{1}{R_1}, & \zeta=0,\tau=0\\ -\dfrac{\tau}{\upsilon R_1}, & \zeta=0,\tau\neq 0\\ \dfrac{\beta_{1,\zeta}K'_{\frac{\tau}{\upsilon}}\left(\beta_{1,\zeta}R_1\right)}{K_{\frac{\tau}{\upsilon}}\left(\beta_{1,\zeta}R_1\right)}, & \zeta\neq 0\end{cases}, \tag{A.5}$$

$$T'^{n,j}_{m,\tau,l}=\begin{cases}\dfrac{(-1)^{\tau}k_0J'_{\tau}\left(k_0R_n\right)H_{m-\tau}\left(k_0R_{nj}\right)\mathrm{e}^{\mathrm{i}\left(m\alpha_{jn}-\tau\alpha_{nj}\right)}}{H_m\left(k_0R_j\right)}, & l=0\\ \dfrac{k_lI'_{\tau}\left(k_lR_n\right)K_{m-\tau}\left(k_lR_{nj}\right)\mathrm{e}^{\mathrm{i}\left(m\alpha_{jn}-\tau\alpha_{nj}\right)}}{K_m\left(k_lR_j\right)}, & l=1,2,3,\cdots\end{cases}. \tag{A.6}$$

3) After inserting Eqs. (20) and (23) into Eq.(28), multiplying both sides by $Z_\zeta(z)\,\mathrm{e}^{-\mathrm{i}\tau\theta_2}$ and integrating for $z\in[-h,0]$ and $\theta_n\in[0,2\pi]$, for any pair of integer (τ,ζ), we have

$$-\sum_{l=0}^{\infty}B_{\tau,l}^{(\chi)}X_{\tau,l}^{(3)}L_{l,\zeta}^{(2)}+hE_{\tau,\zeta}^{\chi,2}\frac{k_\zeta\tilde{K}'_{\tau}\left(k_\zeta R_2\right)}{\tilde{K}_{\tau}\left(k_\zeta R_2\right)}+h\sum_{m=-\infty}^{\infty}E_{m,\zeta}^{\chi,1}T'^{2,1}_{m,\tau,\zeta}=f_{\chi}^{(3)}, \tag{A.7}$$

$$X_{\tau,l}^{(3)}=\begin{cases}\dfrac{|\tau|}{R_2}, & l=0\\ \dfrac{\beta_{2,l}I'_{\tau}\left(\beta_{2,l}R_2\right)}{I_{\tau}\left(\beta_{2,l}R_2\right)}, & l=1,2,3\cdots\end{cases}, \tag{A.8}$$

$$f_{\chi}^{(3)}=\begin{cases}\dfrac{\delta_{\zeta,0}\mathrm{i}^{\tau+1}\mathrm{e}^{\mathrm{i}k_0\left(x_2\cos\beta+y_2\sin\beta\right)}\mathrm{e}^{-\mathrm{i}\tau\beta}gAk_0J'_{\tau}\left(k_0R_2\right)h}{\omega Z_0\left(0\right)}, & \chi=0\\ 0, & \chi=1\\ \dfrac{\delta_{\tau,1}+\delta_{\tau,-1}}{2}I_{\zeta}^{(1)}, & \chi=2\\ \dfrac{-\delta_{\tau,0}R_2}{2\left(h-d_2\right)}I_{\zeta}^{(2)}, & \chi=3\\ \dfrac{\delta_{\tau,1}+\delta_{\tau,-1}}{2}\left(I_{\zeta}^{(3)}-z_0I_{\zeta}^{(1)}\right)+\dfrac{\delta_{\tau,1}+\delta_{\tau,-1}}{16\left(h-d_2\right)}\left(3R_2^2I_{\zeta}^{(2)}-4I_{\zeta}^{(4)}\right), & \chi=4\end{cases}, \tag{A.9}$$

$$I_l^{(1)}=\int_{-d_2}^{0}Z_l\left(z\right)\mathrm{d}z=\begin{cases}\dfrac{\sinh\left(k_0h\right)-\sinh\left[k_0\left(h-d_2\right)\right]}{k_0N_0^{0.5}}, & l=0\\ \dfrac{\sin\left(k_lh\right)-\sin\left[k_l\left(h-d_2\right)\right]}{k_lN_l^{0.5}}, & l=1,2,3,\cdots\end{cases}, \tag{A.10}$$

$$I_l^{(2)}=\int_{-h}^{-d_2}Z_l\left(z\right)\mathrm{d}z=\begin{cases}\dfrac{\sinh\left[k_0\left(h-d_2\right)\right]}{k_0N_0^{0.5}}, & l=0\\ \dfrac{\sin\left[k_l\left(h-d_2\right)\right]}{k_lN_l^{0.5}}, & l=1,2,3,\cdots\end{cases}, \tag{A.11}$$

$$I_l^{(3)}=\int_{-d_2}^{0}Z_l\left(z\right)z\mathrm{d}z$$
$$=\begin{cases}\dfrac{k_0d_2\sinh\left[k_0\left(h-d_2\right)\right]-\cosh\left(k_0h\right)+\cosh\left[k_0\left(h-d_2\right)\right]}{k_0^2N_0^{0.5}}, & l=0\\ \dfrac{k_ld_2\sin\left[k_l\left(h-d_2\right)\right]+\cos\left(k_lh\right)-\cos\left[k_l\left(h-d_2\right)\right]}{k_l^2N_l^{0.5}}, & l=1,2,3,\cdots\end{cases}, \tag{A.12}$$

$$I_l^{(4)}=\int_{-h}^{-d_2}Z_l\left(z\right)\left(z+h\right)^2\mathrm{d}z$$
$$=\begin{cases}\dfrac{k_0^2\left(h-d_2\right)^2\sinh\left[k_0\left(h-d_2\right)\right]-2k_0\left(h-d_2\right)\cosh\left[k_0\left(h-d_2\right)\right]+2\sinh\left[k_0\left(h-d_2\right)\right]}{k_0^3N_0^{0.5}}, & l=0\\ \dfrac{k_l^2\left(h-d_2\right)^2\sin\left[k_l\left(h-d_2\right)\right]+2k_l\left(h-d_2\right)\cos\left[k_l\left(h-d_2\right)\right]-2\sin\left[k_l\left(h-d_2\right)\right]}{k_l^3N_l^{0.5}}, & l=1,2,3,\cdots\end{cases}, \tag{A.13}$$

$$ZZt\left(l\right)=\int_{-d_2}^{0}Z_l\left(z\right)\left(z-z_0\right)\mathrm{d}z$$
$$=\begin{cases}\dfrac{k_0\left(d_2+z_0\right)\sinh\left[k_0\left(h-d_2\right)\right]-\cosh\left(k_0h\right)+\cosh\left[k_0\left(h-d_2\right)\right]-k_0z_0\sinh\left(k_0h\right)}{k_0^2N_0^{0.5}}, & l=0\\ \dfrac{k_l\left(d_2+z_0\right)\sin\left[k_l\left(h-d_2\right)\right]+\cos\left(k_lh\right)-\cos\left[k_l\left(h-d_2\right)\right]-k_lz_0\sin\left(k_lh\right)}{k_l^2N_l^{0.5}}, & l=1,2,3,\cdots\end{cases}, \tag{A.14}$$

4) After inserting Eqs. (12) and (17) into Eq. (29), multiplying both sides by $\cos[\beta_{1,\zeta}(z+h_1)]\cos[\tau(\theta_1-\gamma)/\nu]$ and integrating for $z\in[-h_1,-d_1]$ and $\theta_1\in[\gamma,\gamma+\nu\pi]$, for any pair of integer (τ,ζ), it can be obtained that

$$\sum_{l=0}^{\infty}\left(\frac{\pi}{2}\left(\frac{\mathrm{e}^{\frac{\mathrm{i}\tau\gamma}{\nu}}\tilde{I}_{\frac{\tau}{\nu}}\left(k_lR_{\mathrm{i}}\right)}{k_l\tilde{I}'_{\frac{\tau}{\nu}}\left(k_lR_{\mathrm{i}}\right)}A^{(\chi)}_{\frac{\tau}{\nu},l}+\frac{\mathrm{e}^{-\frac{\mathrm{i}\tau\gamma}{\nu}}\tilde{I}_{-\frac{\tau}{\nu}}\left(k_lR_{\mathrm{i}}\right)}{k_l\tilde{I}'_{-\frac{\tau}{\nu}}\left(k_lR_{\mathrm{i}}\right)}A^{(\chi)}_{-\frac{\tau}{\nu},l}\right)-\mathrm{i}\sum_{\substack{m=-\infty\\ m\nu_0\neq\pm\tau}}^{\infty}\frac{\left(m\nu-\tau\right)\mathrm{e}^{\mathrm{i}(m\nu+\tau)\pi}+\left(m\nu+\tau\right)\mathrm{e}^{\mathrm{i}(m\nu-\tau)\pi}-2m\nu}{2\left(m^2\nu^2-\tau^2\right)}\frac{\mathrm{e}^{\mathrm{i}m\gamma}\tilde{I}_m\left(k_lR_{\mathrm{i}}\right)}{k_l\tilde{I}'_m\left(k_lR_{\mathrm{i}}\right)}A^{(\chi)}_{m,l}\right)L^{(1)}_{\zeta,l}$$
$$=\frac{\pi\left(h_1-d_1\right)}{\varepsilon_\tau\varepsilon_\zeta}\left(X^{(4)}_{\tau,\zeta}C^{(\chi)}_{\tau,\zeta}+Y^{(4)}_{\tau,\zeta}D^{(\chi)}_{\tau,\zeta}\right)+\frac{\delta_{\chi,1}\delta_{\tau,0}\delta_{\zeta,0}\mathrm{i}\pi\left(h_1-d_1\right)}{\rho\omega}$$
, (A.15)

where

$$X^{(4)}_{m,l}=\begin{cases}\left(\dfrac{R_{\mathrm{i}}}{R_1}\right)^{\frac{m}{\nu}}, & l=0\\ \dfrac{I_{\frac{m}{\nu}}\left(\beta_{1,l}R_{\mathrm{i}}\right)}{I_{\frac{m}{\nu}}\left(\beta_{1,l}R_1\right)}, & l\neq0\end{cases};\quad Y^{(4)}_{m,l}=\begin{cases}1+\ln\left(\dfrac{R_{\mathrm{i}}}{R_1}\right), & l=0,m=0\\ \left(\dfrac{R_{\mathrm{i}}}{R_1}\right)^{\frac{m}{\nu}}, & l=0,m\neq0\\ \dfrac{K_{\frac{m}{\nu}}\left(\beta_{1,l}R_{\mathrm{i}}\right)}{K_{\frac{m}{\nu}}\left(\beta_{1,l}R_1\right)}, & l\neq0\end{cases}. \tag{A.16}$$

5) After inserting Eqs. (17) and (23) into Eq. (30), multiplying both sides by

$\cos[\beta_{1,\zeta}(z+h_1)]\cos[\tau(\theta_1-\gamma)/v]$ and integrating for $z\in[-h_1,-d_1]$ and $\theta_1\in[\gamma,\gamma+v\pi]$, for any pair of integer (τ,ζ), we have

$$\sum_{l=0}^{\infty}\left(\frac{\pi}{2}\left(\mathrm{e}^{\frac{\mathrm{i}\tau\gamma}{\upsilon}}E_{\frac{\tau}{\upsilon},l}^{\chi,1}+\mathrm{e}^{\frac{-\mathrm{i}\tau\gamma}{\upsilon}}E_{-\frac{\tau}{\upsilon},l}^{\chi,1}\right)-\mathrm{i}\sum_{\substack{m=-\infty\\|m|\upsilon\neq\tau}}^{\infty}\frac{(m\upsilon-\tau)\mathrm{e}^{\mathrm{i}(m\upsilon+\tau)\pi}+(m\upsilon+\tau)\mathrm{e}^{\mathrm{i}(m\upsilon-\tau)\pi}-2m\upsilon}{2\left(m^2\upsilon^2-\tau^2\right)}\mathrm{e}^{\mathrm{i}m\gamma}E_{m,l}^{\chi,1}\right)L_{\zeta,l}^{(1)}$$

$$+\sum_{m=-\infty}^{\infty}\sum_{l=0}^{\infty}E_{m,l}^{\chi,2}L_{\zeta,l}^{(1)}\left[\frac{\pi}{2}\left(\mathrm{e}^{\frac{\mathrm{i}\tau\gamma}{\upsilon}}T_{m,\frac{\tau}{\upsilon},l}^{1,2}+\mathrm{e}^{\frac{-\mathrm{i}\tau\gamma}{\upsilon}}T_{m,-\frac{\tau}{\upsilon},l}^{1,2}\right)-\mathrm{i}\sum_{\substack{m'=-\infty\\|m'|\upsilon\neq\tau}}^{\infty}\frac{(m'\upsilon-\tau)\mathrm{e}^{\mathrm{i}(m'\upsilon+\tau)\pi}+(m'\upsilon+\tau)\mathrm{e}^{\mathrm{i}(m'\upsilon-\tau)\pi}-2m'\upsilon}{2\left(m'^2\upsilon^2-\tau^2\right)}\mathrm{e}^{\mathrm{i}m'\gamma}T_{m,m',l}^{1,2}\right]$$

$$=\frac{\pi(h_1-d_1)}{\varepsilon_\tau\varepsilon_\zeta}\left(C_{\tau,\zeta}^{(\chi)}+D_{\tau,\zeta}^{(\chi)}\right)+\mathrm{e}^{\mathrm{i}k_0(x_1\cos\beta+y_1\sin\beta)}f_\chi^{(5)}$$

, (A.17)

where

$$T_{m,m',l}^{n,j}=\begin{cases}\dfrac{(-1)^{m'}J_{m'}(k_0R_n)H_{m-m'}(k_0R_{nj})\mathrm{e}^{\mathrm{i}(m\alpha_{jn}-m'\alpha_{nj})}}{H_m(k_0R_j)}, & l=0\\ \dfrac{I_{m'}(k_lR_n)K_{m-m'}(k_lR_{nj})\mathrm{e}^{\mathrm{i}(m\alpha_{jn}-m'\alpha_{nj})}}{K_m(k_lR_j)}, & l=1,2,3,\cdots\end{cases}. \quad (A.18)$$

$$f_\chi^{(5)}=\frac{\mathrm{i}\delta_{\chi,0}gAL_{\zeta,0}^{(1)}}{\omega Z_0(0)}\left(\pi\mathrm{i}^{\frac{\tau}{\upsilon}}\mathrm{e}^{\mathrm{i}\frac{\tau}{\upsilon}\gamma}J_{\frac{\tau}{\upsilon}}(k_0R_1)\cos\left(\frac{\tau}{\upsilon}\beta\right)-\mathrm{i}\sum_{\substack{m=-\infty\\m\upsilon\neq\pm\tau}}^{\infty}\frac{(m\upsilon-\tau)\mathrm{e}^{\mathrm{i}(m\upsilon+\tau)\pi}+(m\upsilon+\tau)\mathrm{e}^{\mathrm{i}(m\upsilon-\tau)\pi}-2m\upsilon}{2\left(m^2\upsilon^2-\tau^2\right)}\mathrm{i}^m\mathrm{e}^{-\mathrm{i}m\beta}\mathrm{e}^{\mathrm{i}m\gamma}J_m(k_0R_1)\right)$$

. (A.19)

6) After inserting Eqs. (20) and (23) into Eq. (31), multiplying both sides by $\cos[\beta_{2,\zeta}(z+h)]\,\mathrm{e}^{-\mathrm{i}\tau\theta_2}$ and integrating for $z\in[-h,0]$ and $\theta_2\in[0,2\pi]$, for any pair of integer (τ,ζ), we have

$$-\frac{h-d_2}{\varepsilon_\zeta}B_{\tau,\zeta}^{(\chi)}+\sum_{l=0}^{\infty}E_{\tau,l}^{\chi,2}L_{\zeta,l}^{(2)}+\sum_{m=-\infty}^{\infty}\sum_{l=0}^{\infty}E_{m,l}^{\chi,1}T_{m,\tau,l}^{2,1}L_{\zeta,l}^{(2)}=f_\chi^{(6)}. \quad (A.20)$$

$$f_\chi^{(6)}=\begin{cases}\dfrac{\mathrm{i}gA}{\omega}\dfrac{\mathrm{i}^\tau J_\tau(k_0R_2)L_{\zeta,0}^{(2)}\mathrm{e}^{\mathrm{i}k_0(x_2\cos\beta+y_2\sin\beta)}\mathrm{e}^{-\mathrm{i}\tau\beta}}{Z_0(0)}, & \chi=0\\ 0, & \chi=1,2\\ \dfrac{\delta_{\tau,0}}{4(h-d_2)}\left[2IZ_\zeta-\delta_{\zeta,0}R_2^2(h-d_2)\right], & \chi=3\\ \dfrac{(\delta_{\tau,1}+\delta_{\tau,-1})R_2}{16(h-d_2)}\left[\delta_{\zeta,0}R_2^2(h-d_2)-4IZ_\zeta\right], & \chi=4\end{cases}. \quad (A.21)$$

$$IZ_\zeta=\int_{-h}^{-d_2}\cos\left[\beta_{2,\zeta}(z+h)\right](z+h)^2\,\mathrm{d}z=\begin{cases}\dfrac{(h-d_2)^3}{3}, & \zeta=0\\ \dfrac{2(-1)^\zeta(h-d_2)^3}{\zeta^2\pi^2}, & \zeta=1,2,3,\cdots\end{cases}. \quad (A.22)$$

Eqs.(A.1), (A.4), (A.8) and (A.11) form a linear algebraic system, which can be used to solve $A_{m,l}^{\chi,n}$, $C_{m,l}^{\chi,n}$, $D_{m,l}^{\chi,n}$ and $E_{m,l}^{\chi,n}$ numerically after truncation. In the present model, the infinite terms of $e^{-im\theta_n}/\cos(m\theta_1/\nu)$, and $Z_l(z)/\cos[\beta_{n,l}(z+h_n)]$ are truncated at $m=M$ and $l=L$, respectively. Accurate results can be obtained by choosing M=12, L=20.

Appendix B. Identity of the optimum wave capture factor over all incidence angles

The total hydrodynamic moment on OB (F_t) relative to the hinge and the total volume flow on OWC (Q_t) can be expressed in matrix notation as [68]

$$\begin{bmatrix} F_t \\ Q_t \end{bmatrix} = \begin{bmatrix} F \\ F_e^{(1)} \end{bmatrix} - \begin{bmatrix} Z & H \\ -H & Y \end{bmatrix} \begin{bmatrix} u \\ p \end{bmatrix}, \tag{B.1}$$

where the first term represents the excitation quantities and the last term the radiation problem. u and p denote the rotation velocity of OB and the air pressure of OWC, respectively. Z, H and Y are hydrodynamic coefficients, which can be decomposed into their real and imaginary parts:

$$Z = R - \mathrm{i}X, \tag{B.2a}$$

$$Y = G - \mathrm{i}B, \tag{B.2b}$$

$$H = C - \mathrm{i}J. \tag{B.2c}$$

Following Falnes [68], Zheng et al. [69], the theoretical maximum power that may be extracted by the OWCOB can be expressed as

$$P_{\mathrm{MAX}}(\beta) = \frac{1}{8}\mathbf{Q}_e^{\dagger}(\beta)\mathbf{S}^{-1}\mathbf{Q}_e(\beta), \tag{B.3}$$

where

$$\boldsymbol{Q}_e = \begin{bmatrix} F \\ -F_e^{(1)} \end{bmatrix}, \text{ and } \mathbf{S} = \begin{bmatrix} R & \mathrm{i}J \\ -\mathrm{i}J & G \end{bmatrix}. \tag{B.4}$$

The theoretical maximum absorbed power as shown in Eq. (B.3) is obtained when an ideal PTO system is applied, such that

$$\begin{bmatrix} u \\ -p \end{bmatrix} = \frac{1}{2}\mathbf{S}^{-1}\boldsymbol{Q}_e. \tag{B.5}$$

Note **S** is a complex Hermitian matrix, which can be written as the product of an upper real triangular matrix **H** and its transpose with the employment of the Cholesky decomposition,

$$\mathbf{S} = \mathbf{H}^{\mathrm{T}}\mathbf{H}, \tag{B.6}$$

hence,

$$\mathbf{S}^{-1} = \mathbf{H}^{-1}\left(\mathbf{H}^{\mathrm{T}}\right)^{-1}. \tag{B.7}$$

For the sake of convenience, a column vector is defined as

$$\boldsymbol{W}(\beta)=\left(\mathbf{H}^{\mathrm{T}}\right)^{-1}\boldsymbol{Q}_{\mathrm{e}}(\beta), \tag{B.8}$$

from which Eq. (B.3) can be rewritten as

$$P_{\mathrm{MAX}}(\beta)=\frac{1}{8}\boldsymbol{W}^{\dagger}(\beta)\boldsymbol{W}(\beta). \tag{B.9}$$

Using the Haskind relation, **S** can be rewritten with the integral of $\boldsymbol{Q}_{\mathrm{e}}$ over all incidence angles as [61]

$$\mathbf{S}=\frac{k}{8\pi\rho g c_{\mathrm{g}}A^{2}}\int_{0}^{2\pi}\boldsymbol{Q}_{\mathrm{e}}(\beta)\boldsymbol{Q}_{\mathrm{e}}^{\dagger}(\beta)\mathrm{d}\beta. \tag{B.10}$$

Multiplying two **H** related inverse matrices results in

$$\left(\mathbf{H}^{\mathrm{T}}\right)^{-1}\mathbf{S}\mathbf{H}^{-1}=\frac{k}{8\pi\rho g c_{\mathrm{g}}A^{2}}\int_{0}^{2\pi}\boldsymbol{W}(\beta)\boldsymbol{W}^{?}(\beta)\mathrm{d}\beta=\mathbf{I}, \tag{B.11}$$

leading to the integral

$$\int_{0}^{2\pi}W_{i}(\beta)W_{j}^{*}(\beta)\mathrm{d}\beta=\delta_{i,j}\frac{8\pi\rho g c_{\mathrm{g}}A^{2}}{k}. \tag{B.12}$$

Integrating Eq. (B.9) over $\beta\in[0,2\pi]$ and adopting Eq. (B.12) gives

$$\int_{0}^{2\pi}P_{\mathrm{MAX}}(\beta)\mathrm{d}\beta=\frac{2\pi\rho g c_{\mathrm{g}}A^{2}}{k}, \tag{B.13}$$

and

$$\frac{1}{2\pi}\int_{0}^{2\pi}\eta_{\mathrm{MAX}}(\beta)\mathrm{d}\beta=\frac{k}{\pi\rho g c_{g}A^{2}}\int_{0}^{2\pi}P_{\mathrm{MAX}}(\beta)\mathrm{d}\beta=2. \tag{B.14}$$

References

[1] Drew B, Plummer AR, Sahinkaya MN. A review of wave energy converter technology. P I Mech Eng a-J Pow. 2009;223:887-902.

[2] Lund H. Renewable energy strategies for sustainable development. Energy. 2007;32:912-9.

[3] Astariz S, Iglesias G. The economics of wave energy: A review. Renew Sust Energ Rev. 2015;45:397-408.

[4] Clément A, McCullen P, Falcão A, Fiorentino A, Gardner F, Hammarlund K, et al. Wave energy in Europe: current status and perspectives. Renew Sust Energ Rev. 2002;6:405-31.

[5] Falcão AFdO. Wave energy utilization: A review of the technologies. Renew Sust Energ Rev.

2010;14:899-918.
[6] Lehmann M, Karimpour F, Goudey CA, Jacobson PT, Alam MR. Ocean wave energy in the United States: Current status and future perspectives. Renew Sust Energ Rev. 2017;74:1300-13.
[7] Falcão AFdO, Henriques JCC. Oscillating-water-column wave energy converters and air turbines: A review. Renew Energ. 2016;85:1391-424.
[8] Heath TV. A review of oscillating water columns. Philos T R Soc A. 2012;370:235-45.
[9] Evans DV, Porter R. Hydrodynamic characteristics of an oscillating water column device. Applied Ocean Research. 1995;17:155-64.
[10] Rezanejad K, Bhattacharjee J, Guedes Soares C. Stepped sea bottom effects on the efficiency of nearshore oscilating water column device. Ocean Eng. 2013;70:25-38.
[11] Ning DZ, Shi J, Zou QP, Teng B. Investigation of hydrodynamic performance of an OWC (oscillating water column) wave energy device using a fully nonlinear HOBEM (higher-order boundary element method). Energy. 2015;83:177-88.
[12] Zhang Y, Zou QP, Greaves D. Air-water two-phase flow modelling of hydrodynamic performance of an oscillating water column device. Renew Energ. 2012;41:159-70.
[13] Pereiras B, López I, Castro F, Iglesias G. Non-dimensional analysis for matching an impulse turbine to an OWC (oscillating water column) with an optimum energy transfer. Energy. 2015;87:481-9.
[14] López I, Pereiras B, Castro F, Iglesias G. Holistic performance analysis and turbine-induced damping for an OWC wave energy converter. Renew Energ. 2016;85:1155-63.
[15] Morris-Thomas MT, Irvin RJ, Thiagarajan KP. An investigation into the hydrodynamic efficiency of an oscillating water column. Journal of Offshore Mechanics and Arctic Engineering. 2007;129:273-8.
[16] Viviano A, Naty S, Foti E, Bruce T, Allsop W, Vicinanza D. Large-scale experiments on the behavior of a generalized Oscillating Water Column under random waves. Renew Energ. 2016;99:875-87.
[17] Pawitan KA, Dimakopoulos AS, Vicinanza D, Allsop W, Bruce T. A loading model for an OWC caisson based upon large-scale measurements. Coast Eng. 2019;145:1-20.
[18] López I, Carballo R, Taveira-Pinto F, Iglesias G. Sensitivity of OWC performance to air compressibility. Renew Energ. 2019;in press.
[19] López I, Carballo R, Iglesias G. Site-specific wave energy conversion performance of an oscillating water column device. Energy Conversion and Management. 2019;195:457-65.
[20] Rezanejad K, Bhattacharjee J, Guedes Soares C. Analytical and numerical study of nearshore multiple oscillating water columns. Journal of Offshore Mechanics and Arctic Engineering. 2016;138.
[21] Rezanejad K, Bhattacharjee J, Guedes Soares C. Analytical and numerical study of dual-chamber oscillating water columns on stepped bottom. Renew Energ. 2015;75:272-82.
[22] Ning DZ, Wang RQ, Chen LF, Sun K. Experimental investigation of a land-based dual-chamber OWC wave energy converter. Renew Sust Energ Rev. 2019;105:48-60.
[23] Arena F, Romolo A, Malara G, Ascanelli A. On design and building of a U-OWC wave energy converter in the Mediterranean Sea: a case study. International Conference on Offshore Mechanics and Arctic Engineering. Nantes, France2013.
[24] Malara G, Arena F. Analytical modelling of an U-Oscillating Water Column and performance in random waves. Renew Energ. 2013;60:116-26.
[25] Arena F, Romolo A, Malara G, Fiamma V, Laface V. The first full operative U-OWC plants in the port of Civitavecchia. ASME 2017 36th International Conference on Ocean, Offshore and Arctic Engineering. Trondheim, Norway2017. p. 11.
[26] Malara G, Romolo A, Fiamma V, Arena F. On the modelling of water column oscillations in U-OWC

energy harvesters. Renew Energ. 2017;101:964-72.
[27] Martins-rivas H, Mei CC. Wave power extraction from an oscillating water column at the tip of a breakwater. Journal of Fluid Mechanics. 2009;626:395-414.
[28] Martins-rivas H, Mei CC. Wave power extraction from an oscillating water column along a straight coast. Ocean Eng. 2009;36:426-33.
[29] Lovas S, Mei CC, Liu YM. Oscillating water column at a coastal corner for wave power extraction. Applied Ocean Research. 2010;32:267-83.
[30] Zheng S, Zhang Y, Iglesias G. Coast/breakwater-integrated OWC: A theoretical model. Mar Struct. 2019;66:121-35.
[31] Zheng S, Antonini A, Zhang Y, Greaves D, Miles J, Iglesias G. Wave power extraction from multiple oscillating water columns along a straight coast. Journal of Fluid Mechanics. 2019;878:445-80.
[32] Howe D, Nader JR. OWC WEC integrated within a breakwater versus isolated: Experimental and numerical theoretical study. International Journal of Marine Energy. 2017;20:165-82.
[33] Evans DV. The oscillating water column wave-energy device. IMA Journal of Applied Mathematics. 1978;22:423-33.
[34] Evans DV. Wave-power absorption by systems of oscillating surface pressure distributions. Journal of Fluid Mechanics. 1982;114:481-99.
[35] Luo Y, Wang Z, Peng G, Xiao Y, Zhai L, Zhang Q. Numerical simulation of a heave-only floating OWC (oscillating water column) device. Energy. 2014;76:799-806.
[36] Elhanafi A, Fleming A, Macfarlane G, Leong Z. Underwater geometrical impact on the hydrodynamic performance of an offshore oscillating water column-wave energy converter. Renew Energ. 2017;105:209-31.
[37] He F, Zhang H, Zhao J, Zheng S, Iglesias G. Hydrodynamic performance of a pile-supported OWC breakwater: An analytical study. Applied Ocean Research. 2019;88:326-40.
[38] Elhanafi A, Macfarlane G, Ning D. Hydrodynamic performance of single–chamber and dual–chamber offshore–stationary Oscillating Water Column devices using CFD. Applied Energy. 2018;228:82-96.
[39] He F, Huang Z, Law AWK. An experimental study of a floating breakwater with asymmetric pneumatic chambers for wave energy extraction. Applied Energy. 2013;106:222-31.
[40] He F, Huang Z, Law AWK. Hydrodynamic performance of a rectangular floating breakwater with and without pneumatic chambers: An experimental study. Ocean Eng. 2012;51:16-27.
[41] Evans DV, Porter R. Efficient calculation of hydrodynamic properties of OWC-type devices. Journal of Offshore Mechanics and Arctic Engineering. 1997;119:210-8.
[42] Sheng W, Alcorn R, Lewis A. Assessment of primary energy conversions of oscillating water columns. I. Hydrodynamic analysis. J Renew Sustain Ener. 2014;6:053113.
[43] Sheng W, Alcorn R, Lewis A. Assessment of primary energy conversions of oscillating water columns. II. Power take-off and validations. J Renew Sustain Ener. 2014;6:053114.
[44] Nader JR. Interaction of ocean waves with oscillating water column wave energy convertors. Wollongong: University of Wollongong; 2013.
[45] Konispoliatis DN, Mavrakos SA. Hydrodynamic analysis of an array of interacting free-floating oscillating water column (OWC's) devices. Ocean Eng. 2016;111:179-97.
[46] Deng ZZ, Huang ZH, Law AWK. Wave power extraction by an axisymmetric oscillating-water-column converter supported by a coaxial tube-sector-shaped structure. Applied Ocean Research. 2013;42:114-23.

[47] Wu B, Chen T, Jiang J, Li G, Zhang Y, Ye Y. Economic assessment of wave power boat based on the performance of “Mighty Whale” and BBDB. Renew Sust Energ Rev. 2018;81:946-53.
[48] Sheng W. Power performance of BBDB OWC wave energy converters. Renew Energ. 2019;132:709-22.
[49] Correia da Fonseca FX, Gomes RPF, Henriques JCC, Gato LMC, Falcão AFO. Model testing of an oscillating water column spar-buoy wave energy converter isolated and in array: Motions and mooring forces. Energy. 2016;112:1207-18.
[50] Elhanafi A, Macfarlane G, Fleming A, Leong Z. Experimental and numerical measurements of wave forces on a 3D offshore stationary OWC wave energy converter. Renew Energ. 2017;144:98-117.
[51] Ning D, Zhou Y, Zhang C. Hydrodynamic modeling of a novel dual-chamber OWC wave energy converter. Applied Ocean Research. 2018;78:180-91.
[52] Wu J, Yao Y, Sun D, Ni Z, Goteman M. Numerical and experimental study of the Solo Duck wave energy converter. Energies. 2019;12:1941.
[53] Cruz J. Ocean Wave Energy: current status and future prespectives. Berlin: Springer; 2008.
[54] Cruz JMBP, Salter SH. Numerical and experimental modelling of a modified version of the Edinburgh Duck wave energy device. Proceedings of the Institution of Mechanical Engineers, Part M: Journal of Engineering for the Maritime Environment. 2006;220:129-47.
[55] Nambiar AJ, Forehand DIM, Kramer MM, Hansen RH, Ingram DM. Effects of hydrodynamic interactions and control within a point absorber array on electrical output. International Journal of Marine Energy. 2015;9:20-40.
[56] Haren P. Optimal design of Hagen-Cockerell rafts: Massachusetts Institute of Technology; 1978.
[57] Yang J, Zhang DH, Chen Y, Liang H, Tan M, Li W, et al. Design, optimization and numerical modelling of a novel floating pendulum wave energy converter with tide adaptation. China Ocean Eng. 2017;31:578-88.
[58] Jakobsen MM, Beatty S, Iglesias G, Kramer MM. Characterization of loads on a hemispherical point absorber wave energy converter. International Journal of Marine Energy. 2016;13:1-15.
[59] Ransley EJ, Greaves DM, Raby A, Simmonds D, Jakobsen MM, Kramer M. RANS-VOF modelling of the Wavestar point absorber. Renew Energ. 2017;109:49-65.
[60] Zheng S, Zhang Y. Analytical study on wave power extraction from a hybrid wave energy converter. Ocean Eng. 2018;165:252-63.
[61] Zheng S, Zhang Y. Theoretical modelling of a new hybrid wave energy converter in regular waves. Renew Energ. 2018;128A:125-41.
[62] Zheng S, Zhang Y, Iglesias G. Wave-structure interaction in hybrid wave farms. J Fluid Struct. 2018;83:386-412.
[63] Goda Y. Random seas and design of maritime structures. Singapore: World Scientific; 2000.
[64] Yeung RW. Added mass and damping of a vertical cylinder in finite-depth waters. Applied Ocean Research. 1981;3:119-33.
[65] Zheng S, Zhu G, Simmonds D, Greaves D, Iglesias G. Wave power extraction from a tubular structure integrated oscillating water column. Renew Energ. 2020;150:342-55.
[66] Michele S, Renzi E, Perez-Collazo C, Greaves D, Iglesias G. Power extraction in regular and random waves from an OWC in hybrid wind-wave energy systems. Ocean Eng. 2019;191:106519.
[67] Michele S, Sammarco P, d'Errico M. Theory of the sychronous motion of an array of floating flap gates oscillating wave surge converter. P Roy Soc a-Math Phy. 2016;472:20160174.
[68] Falnes J. Ocean Waves and Oscillating Systems: Linear Interaction Including Wave-energy Extraction.

Cambridge, UK: Cambridge University Press; 2002.
[69] Zheng S, Zhang Y, Iglesias G. Power capture performance of hybrid wave farms combining different wave energy conversion technologies: the H-factor. Energy. 2020;204:117920.